Size and build strategy effects for the L-PBF process applied to Inconel 625 vertical struts: a combined numerical and experimental approach

Patrice Peyre, Julien Rodrigues da Silva, Zehoua Hadjem-Hamouche, Anne-Laure Helbert, Julien Daligault, Morgan Dal, Frédéric Coste, Thierry Baudin

Size and build strategy effects for the L-PBF process applied to Inconel 625 vertical struts: a combined numerical and experimental approach

Patrice Peyre[1] · Julien Rodrigues Da Silva[1,2] · Zehoua Hamouche[1] · Anne-Laure Helbert[2] · Julien Daligault[1] · Morgan Dal[1] · Frédéric Coste[1] · Thierry Baudin[2]

Abstract

A combined numerical and experimental analysis of melt pool dimensions and resulting solidification conditions was carried out on small laser powder bed fusion (L-PBF) struts (0.2- to 2-mm diameters), considered as single constitutive parts of the structure lattice. In the beginning, the high-speed imaging monitoring of melt pools was performed on a dedicated instrumented L-PBF set-up for various scan strategies. In the subsequent stage, a numerical thermal model was employed on COMSOL Multiphysics® to determine the alteration of the melt pool by the struts' diameter and scanning strategy for constant (power, scan speed) conditions. A good agreement was obtained between experimental and numerical melt pool areas. This allowed validation of calculated local cooling rates and thermal gradients near the solidification front. A clear difference was shown between outside-in or inside-out strategies and contour-hatching in terms of local solidification conditions. Higher cooling rates were obtained for outside-in conditions, especially near the external part of struts whereas inside-out conditions promoted more uniform cooling rates and thermal gradients. Moreover, a reduction of strut diameter induced the formation of a single melt pool on the full strut's surface, which promoted lower and more uniform cooling rates and a highly textured built material. A fairly good agreement was found between simulated thermal data and local microstructure development at the scale of solidification cells. Finally, the current work provides a deeper understanding of size and L-PBF strategy versus microstructure formation and allows adapting build conditions on strut diameters.

Keywords Modeling · L-PBF · Laser · Scan strategy · Microstructures · Struts

1 Introduction

Additive manufacturing (AM) with lasers is now a recognized tool for building more or less complex shapes on a large range of dimensions, mostly comprised between less than 1 mm and a few meters, depending on the kind of AM process (powder bed fusion, direct energy deposition, etc.). Among laser AM processes, laser powder bed fusion (L-PBF) provides higher complexity combined with better spatial resolution and allows building parts ranging between less than 0.5 mm and more than 50 cm for the more recent industrial L-PBF developments [1]. The smaller L-PBF parts include, for instance, the cylindrical strut components of lattice structures, for which, thanks to topology optimization, a large range of architectured or hybrid (solid/architectured) parts are currently designed and manufactured, with many potential applications such as biomedical ones [2]. On the one hand, the mechanical resistance of such architectured materials has already been widely investigated at a global scale, for instance, for reaching high damping properties [3], or tuned to provide innovative mechanical properties through dedicated lattice structures [4]. On the other hand, the influence of L-PBF single strut size on their microstructure and mechanical strength has been investigated only in a limited number of recent studies, with various assumptions concerning the thermal origin of induced microstructural variations, and discrepancies in mechanical results. For instance, [5] and [6] on Ti6Al4V indicate a progressive increase in yield strength with a decrease in strut's diameters (between 2 and 0.3 mm), whereas [7] has shown a clear decrease of yield

✉ Patrice Peyre
patrice.peyre@ensam.eu

[1] PIMM Laboratory, Arts Et Métiers Institute of Technology, CNRS, CNAM, HESAM University, 151 Bd de l'Hôpital, 75013 Paris, France

[2] ICMMO, University Paris-Saclay, CNRS, 17 Av. Des Sciences, 91190 Orsay, France

strength for small diameters on 316L, partially due to larger solidification cells. In all these studies, the columnar grain width did not change with strut diameter, whereas modifications of solidification cells have been widely reported. All these works also confirm lower elongation rates for small struts, due to the dominant influence of pores.

Most of these works, such as Barba et al. on Ti6Al4V [6] or Wang et al. [7] and Britt et al. [8] on 316L indicate a microstructural refinement for the smaller struts' diameters, assumed to be due to faster cooling rates. Smaller solidification cells (316L) or α-laths (Ti6Al4V) are shown on small struts. Simultaneously, more elongated grains along the build direction combined with a pronounced fiber texture are obtained, due to stronger epitaxial growth.

However, little attention was paid to a deep physical understanding of the influence of small L-PBF part size, especially considering the influence of specific thermal boundary conditions (powder beds with low thermal conductivity) surrounding parts under construction. To address such a problem, the combined use of simplified modeling and in situ monitoring seems to be an interesting way.

Many numerical approaches are possible at different working scales to address the various physical features of L-PBF, as indicated by Soundararajan et al. in their state of the art [9].

At a microscale and mesoscale, multiphysics thermal and hydrodynamic modeling provide a physical representation of L-PBF melt pools. This involves for instance the keyhole mode formation including a realistic laser-matter interaction with the deformed liquid surface using, for instance, a ray tracing approach [10], or the overlapping of a few tracks to address lack-of-fusion or roughness formation. Such models can either consider the powder bed as an equivalent medium or directly consider powder grains as discrete media [11] and address their incorporation in the melt pool. However, they are restricted to a limited number of fusion tracks due to the high computational times of fully coupled models.

At a macro scale, thermo-mechanical models using more or less complex laser heat sources have been attempted to calculate residual stresses and distortions, through a simplified determination of temperature history in activated layers [12].

Concerning the selection of microstructures, CAFE (cellular automaton finite element) simulations have also been used for calculating L-PBF solidification microstructures. They have been used initially for welding [13] and applied recently to additive manufacturing by various authors including Camus et al. [14] and Ma et al. [15] on 316L steel.

Simplified approaches such as analytical models were also used to provide a rough estimation of cooling conditions. For instance, Scipioni Bertoli et al. [16] estimated cooling rates on 316L with the use of the Rosenthal equation for laser melting and established a correlation between the diameter of L-PBF solidification cells δ and local cooling rate V_c as follows: $\delta = \beta . V_c^{-0.33}$ (with $\beta \sim$ average grain size). A similar formulation was used by Li et al. [17] on Inconel 625 to estimate cooling rates from the experimental measurement of average cell diameters.

The finite element simulation of rather large and complex L-PBF parts is a real issue, due to large computation times, even if efforts have been made to combine high spatial resolution with acceptable time scales like for instance some recent 3D thermal modeling by Olleak et al. [18, 19] on centimeter-scale parts.

Compared with larger build parts, for which significant CPU time is required, the modeling of L-PBF applied to small struts has less computational cost than larger samples. Moreover, investigating the influence of strut size is scientifically interesting to address due to the balance between laser heat input and a more or less constrained thermal dissipation, which is highly strut size dependent. The resulting struts' microstructures, which vary with strut diameter [6, 8], necessitate a numerical determination of local temperature history near the melt pool limit, which is highly complex to obtain experimentally, due to the high requested spatial resolution.

Promoppatum et al. [20] have carried out an interesting numerical thermo-metallurgical modeling of small L-PBF struts, including size effects, and take into account solid phase transformation. They have confirmed numerically the reduction of Ti-α lath width with a decrease of diameters and predicted with a correct agreement the resulting increase of yield strength. However, they did not confront thermal data and/or melt pool dimensions with experimental values and they did not address the influence of build strategy.

More widely, such modeling works, are usually confronted with time-resolved experiments like x-ray radiography during L-PBF fusion as shown by [21], real-time temperature signatures of melt pools [22, 23], or post-mortem data, but there is still a lack of in-operando experimental data and experimental techniques for validating numerical models, especially at the melt pool scale.

Several recent studies have already investigated the L-PBF process stability on homemade and open L-PBF setups. One can mention the analysis of spatter generation [24] or the influence of work pressure on melt pool dynamics

Table 1 Thermo-physical properties of Inconel 625 [28]

T (K)	C_p (J·kg^{-1}·K^{-1})	ρ (kg/m^3)	k (W·m^{-1}·K^{-1})
293	450	8440	10
473	470	8380	12
673	500	8290	16
873	550	8200	20
1273	620	7930	25
$1570 = T_{sol}$	650	7670	29
$1640 = T_{liq}$	710	7350	50
2200	710	7350	80
2500	710	7350	80

Table 2 Constant L-PBF conditions considered in all the work

Parameters	Values
P_0 (W)	125
V_0 (m/s)	0.5
Laser diameter D_{las} (µm)	70
Hatch distance H (µm)	120
Offset contour distance (µm)	80

Table 3 FE mesh parameters for the two models

Model	*Area*	*Values*
GMLM	1- activated layers	D_{strut} × 0.05 mm height
	Maximum mesh size	80 µm
	2- cylindrical substrate	D_{strut} × 3.5 mm height
	Mesh size (transition zone)	100 µm
	Maximum mesh size	300 µm
HRSLM	1- Heat affected layer	D_{strut} × 0.125 mm height
	Maximum mesh size	20 µm
	2- cylindrical substrate	D_{strut} × 1.25 mm height
	Mesh size (transition zone)	50 µm
	Maximum mesh size	300 µm

[25], but rather few studies have considered a sufficient spatial resolution to provide reliable data on melt pool areas.

The current work proposes a comprehensive study of strut size and build strategy effects including a 3D simplified thermal modeling for L-PBF Inconel 625 struts having 0.2- to 2-mm diameters, combined with experimental validation of melt pool dimensions for various scan strategies. The analysis of strut-like samples is useful not only as structure lattice constituents allowing attractive engineering properties but also as supporting structures for any L-PBF manufacturing.

Inconel 625 was selected as a key material for investigating numerically and experimentally L-PBF-built struts' properties because of its high strength, stiffness, and oxidation resistance at high temperatures, which allows envisaging it for architectured materials like heat exchangers or energy absorbers [26].

2 The numerical model

The local thermal history of L-PBF parts is usually composed of one to four fast melting-solidification cycles, with cooling rates between 10^5 and 10^6 K/s followed by a longer and quasi-stationary tempering treatment at T_0 mean temperature. This T_0 is highly dependent on the laser power (P_0), scan speed (V_0), hatch distance (H), and layer height (Δh) parameters for a constant laser diameter D_{las}. It also depends on the time pause (t_p) between subsequent layers, which mostly increases with the number of building parts on the plateau. Such a time pause is usually comprised of between 30 and 120 s for usual L-PBF conditions. Additionally, the build dimension and the number of scan tracks per layer can both play a significant role in local thermal cycles $T = f(x, y, z, t)$ and induced microstructures.

To fulfill the requirements of such a model, a two-step approach derived from Promoppatum et al.'s work [20] is proposed:

– First, global modeling is carried out, to record average struts' temperatures T_{temp}, their variation with strut diameter, and scan strategy. This model activates up to ten layers of 50 µm height thanks to the *linear elastic module

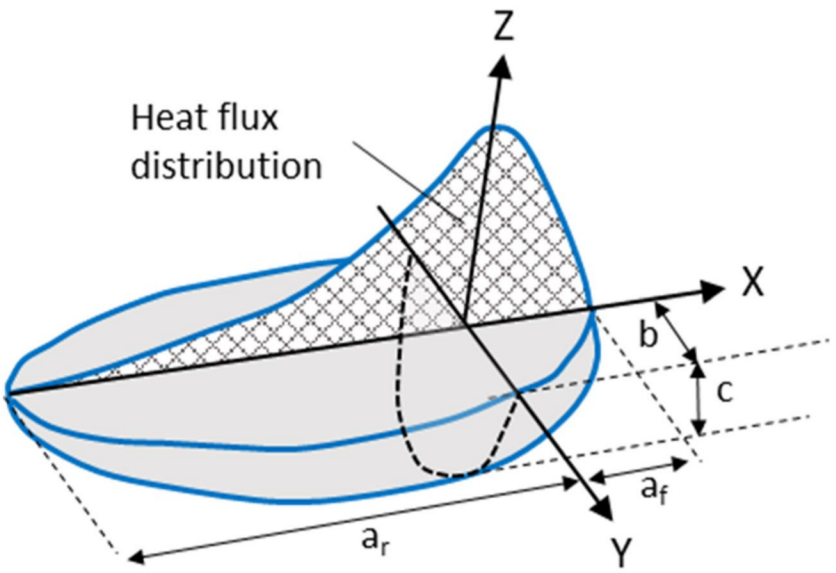

Fig. 1 Goldak double ellipsoid heat source (in the current work, $a_r = a_f = b = r_{las}$)

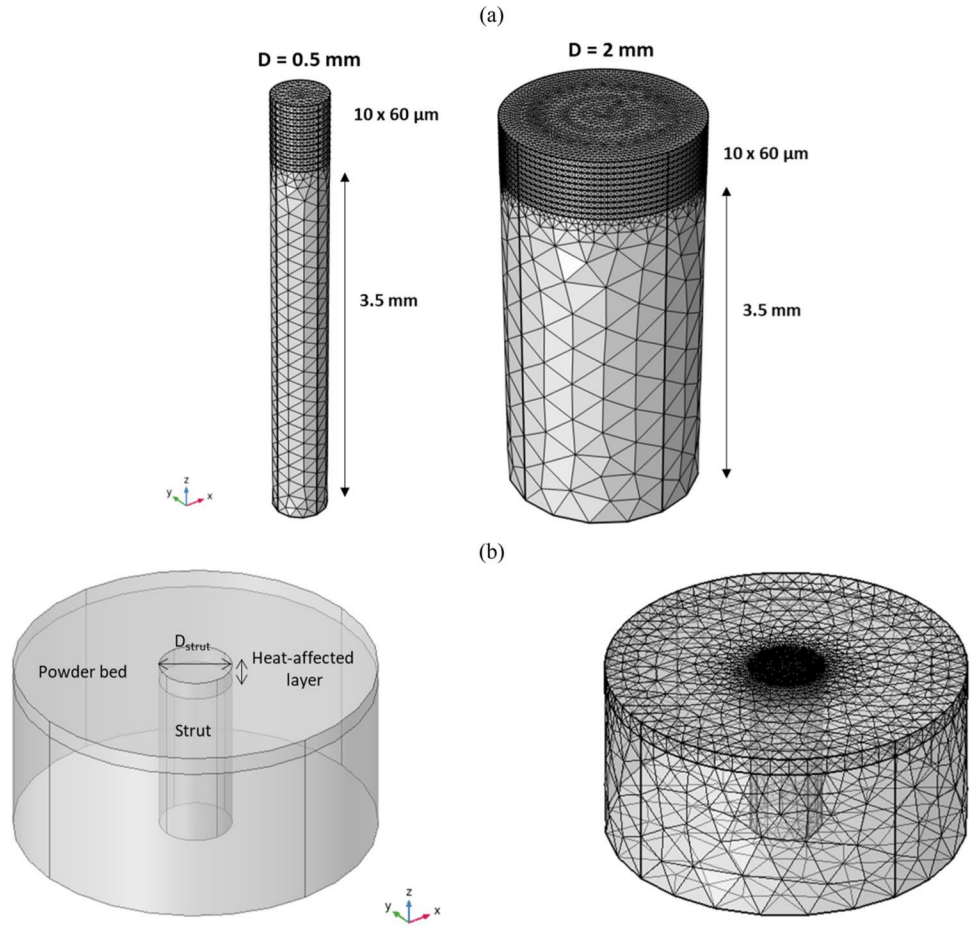

Fig. 2 Geometrical domains corresponding to **a** the GMLM model (example of 0.5-mm and 2-mm strut diameters) (ten layers to be activated on a 4-mm-height cylinder) and **b** the single-layer SLM model (case of a 0.5-mm strut surrounded by a powder bed, with a high mesh density in the 0.125-mm-thick upper heat affected layer)

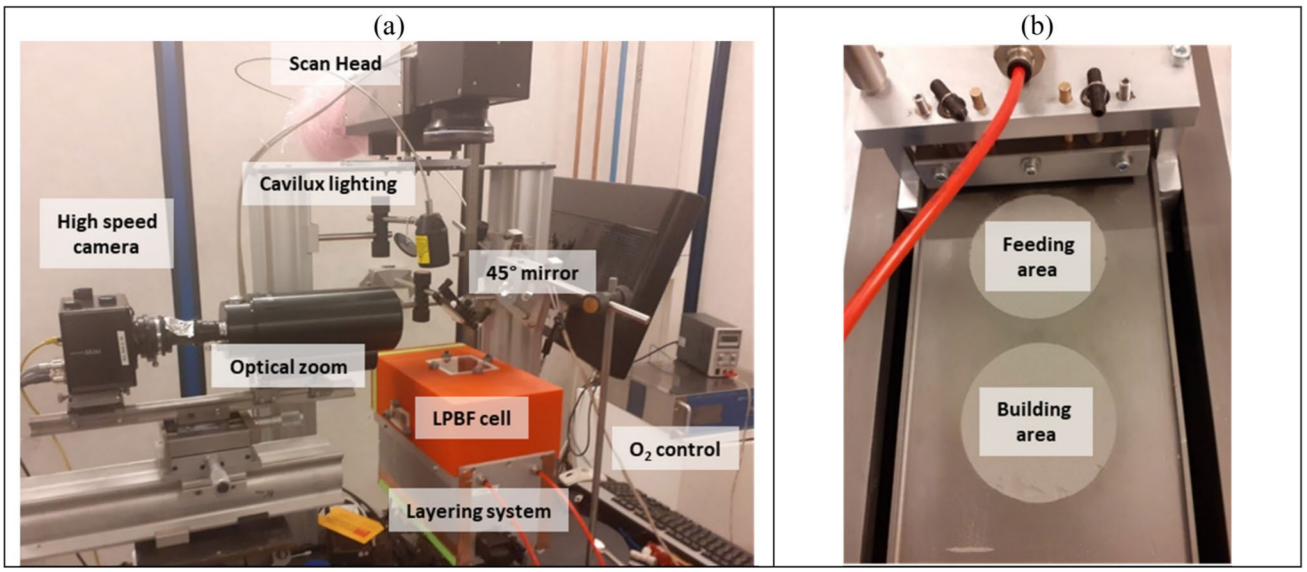

Fig. 3 Open-architecture L-PBF set-up with high-speed imaging device: **a** global view and **b** top view

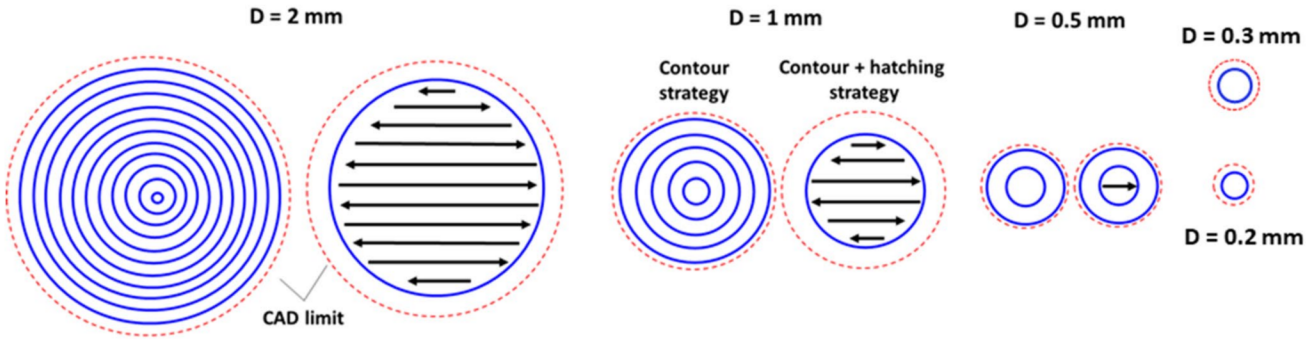

Fig. 4 Scan strategies vs strut diameters

Table 4 Computational domains and used building strategy for a pure contouring mode (C_I or C_O) with an 80-µm offset contour distance

	GMLM (10 layers)	HRSLM (1 layer)	Number of contours
0.2 mm	2760	33,269 elements	1
0.3 mm	3206	43,179 elements	1
0.5 mm	4370	76,096 elements	3
1 mm	12,820	240,888 elements	5
2 mm	117,334	1,003,152 elements	11

of COMSOL Multiphysics®. This first model is called the global multilayer model (GMLM).

– Second, considering a single built layer at the right T_{temp} temperature as an initial condition, a more detailed model (with a higher mesh resolution) is used to estimate precisely melt pool features, to compare them with experimental data, and to deduce accurately local cooling and solidification kinetics. This model is called the high-resolution single-layer model (HRSLM).

The two finite element models do not consider hydrodynamic flow in the molten metal, which is assumed to be a strong limitation for a precise determination of solidification conditions. However, due to extensive calculation time, a fully coupled thermal + hydrodynamic calculation could not be carried out on long scan tracks (several cm for $D = 2$ mm) such as those considered in the current work. Moreover, a unique laser irradiance in terms of laser power P_0, scan speed V_0, and spot diameter D_{las} is considered in all the work, which allows the use of a unique equivalent heat source (Goldak [27]) calibrated with experiments, including indirectly the thermal influence of convection flow.

One has to mention that, apart from the surrounding equivalent medium, whose thermal properties have been adjusted to represent the powder bed, the fusion has been considered on a solid surface and not on discrete powder grains. However, as mentioned by Scipioni Bertoli et al. [16], the powder bed can be ignored in the calculation of L-PBF since it has no significant effect on the final result.

Calculations are carried out with COMSOL Multiphysics® software, considering the thermal module for solving heat equations in transient conditions and the linear elastic module for layer activation. A 1.8-GHz laptop equipped with 8 cores and an 8 Go RAM is used, and nonlinear material properties are considered (Table 1), including latent heat

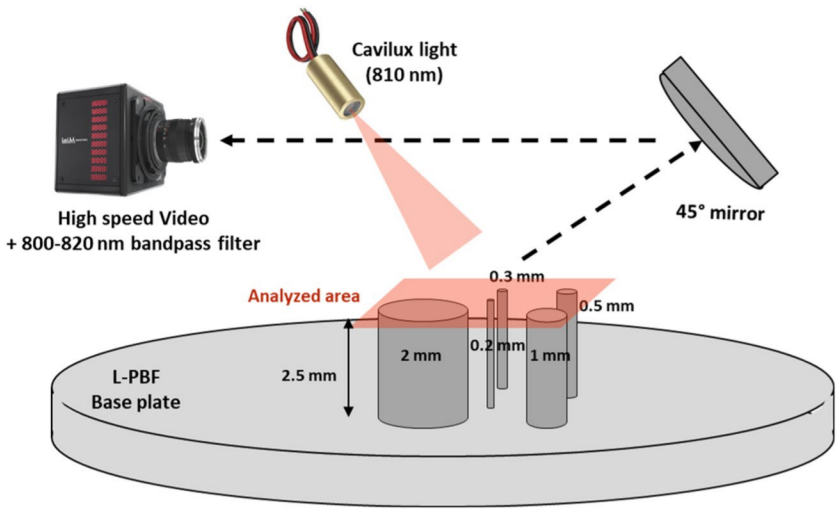

Fig. 5 Experimental procedure of high-speed imaging

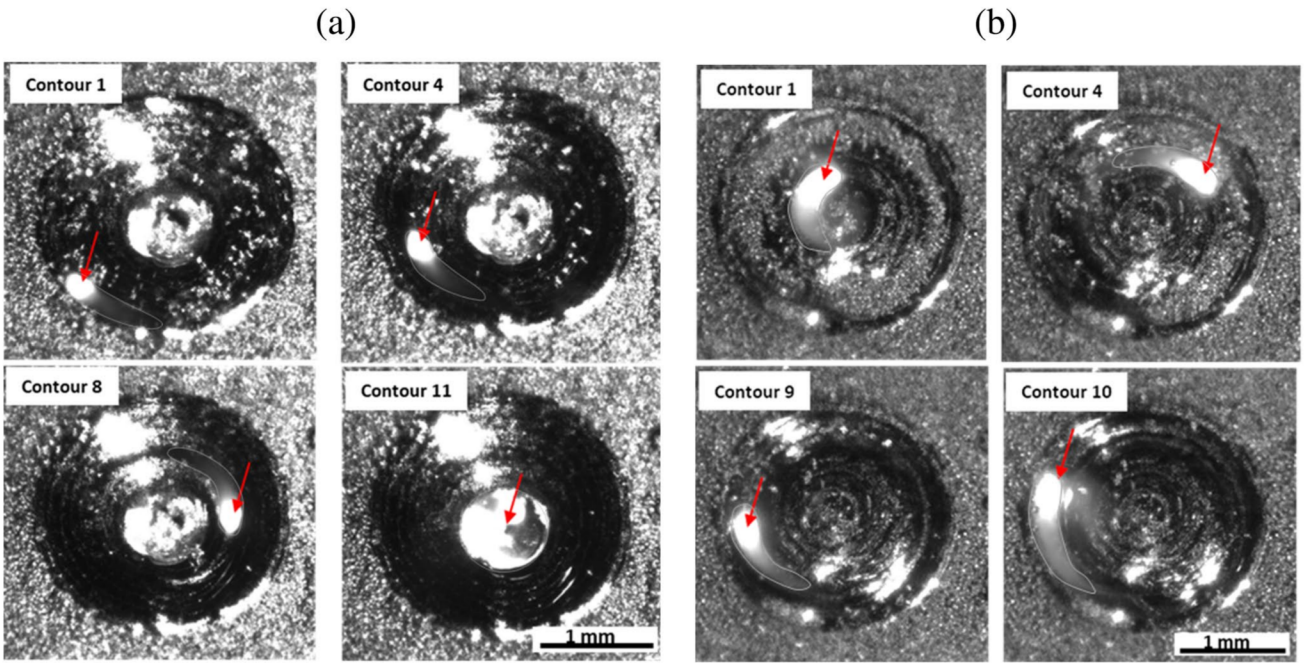

Fig. 6 Top view of struts and melt pools during L-PBF with $P = 125$ W – V = 0.5 m/s (2 mm cylinder, at four distinct contouring times). **a** OI strategy. Melt pools are indicated with the red arrow and their contour is delimited by a grey line. The last melt pool (contour 11) is a circular metal droplet surrounded by solidified areas. **b** IO strategy. Melt pools are larger at the onset (contour 1) and the end of fusion (contour 10)

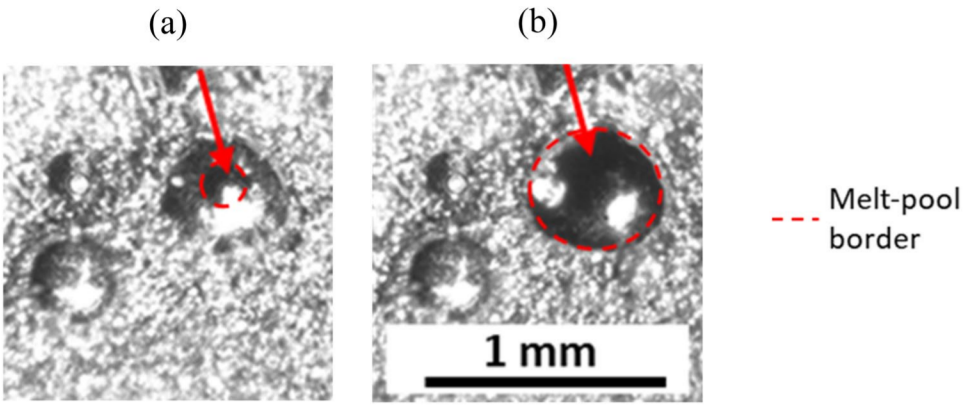

Fig. 7 Powder bed fusion of the 0.5-mm strut (right strut, melt pools indicated with the red arrow) with $P = 125$ W – V = 0.5 m/s (I-O strategy). **a** At the onset of melting (top of the (n-1)th solidified layer). **b** When the 0.5-mm strut surface is completely melted during contouring of the nth layer and a near-round fusion zone is evidenced

of fusion L_m (J·kg^{-1}), incorporated in the formulation of specific heat C_p (J·kg^{-1}·K^{-1}) as shown here below (Eq. 1).

To consider a 50% powder bed compactness in the HRSLM model, we have used (k_{Powder} (T) ~ 0.05 k_{Solid} (T) following previous works by [10]),$C_{p,Powder}$ (T) = $C_{p,\,Solid}$(T) and ρ_{Powder} (T) = 0.5 ρ_{Solid} (T).

$$C_p = C_p(\mathrm{T}) + \exp\left(-\frac{(T - T_m)^2}{dT^2}\right) \cdot \frac{1}{\sqrt{\pi . dT^2}} \cdot L_m \qquad (1)$$

where dT is the solidification range (= 70 K), T_m is the melting temperature, and L_m is the latent heat of fusion (= 3.10^5 J·kg^{-1}).

2.1 Heat source

The hydrodynamic flow is not considered in the calculation, but an equivalent volumetric heat source (Goldak's ellipsoid) is used to simplify calculations and provide realistic melt pool sizes. A unique Goldak distribution is then calibrated for all the calculations, thanks to single L-PBF tracks. Such an assumption is justified because laser power P_0, scan speed V_0, and laser diameter D_{las} are kept constant in all the work (see Table 2). To provide a further simplification to the volumetric deposit, a single ellipsoid is considered (Fig. 1), without distinction between the front and rear laser

power deposit ($a_r = a_f = a = r_{laser}$), in agreement with recent modeling works by Baumard et al. [29].

For a given strut diameter, only scan strategies are varied, using (1) either a pure contouring strategy, with outside-in (OI) or inside-out (IO) modes (2) or a 1 contour + parallel hatch lines strategy (called CH strategy) conventionally used for L-PBF manufacturing of larger parts. The displacement of the heat source is imposed thanks to a change of origin of the (x_0, y_0) starting laser position, as shown in Eq. 3 for a linear scan used in the CH strategy. For the OI and IO contour strategies, (x_0, y_0) positions are varied with the use of circular equations such as $x = x - r_n * \cos(\theta_n)$ and $y = y - r_n * \sin(\theta_n)$ where r_n is the radius of n-th contour and $\theta_n = V/r_n$ is the rotation angle.

$$\rho C_p \frac{\partial T}{\partial t} = \nabla(k.\nabla T) + Q_{vol} \tag{2}$$

$$Q_{vol}(x,y,z) = \left(\frac{6\sqrt{3}AP_0}{abc}\right).\exp\left(-3\left(\frac{(y-y_0)^2}{b^2} + \frac{(x-V_0t-x_0)^2}{a^2} + \frac{(z-z_0)^2}{c^2}\right)\right) \tag{3}$$

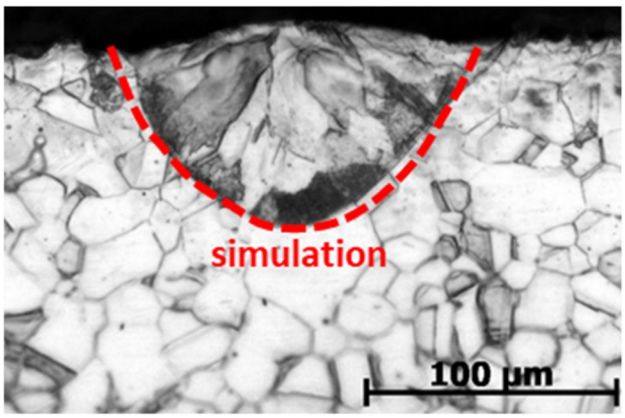

Fig. 8 Calibration of Goldak source parameters on a single L-PBF track (125 W – 0.5 m/s). The best-simulated isotherm is obtained with $a_f = a_r = b = 35$ µm and $c = 70$ µm

$$q_{loss} = h\left(T - T_{surf}\right) + \varepsilon\sigma(T^4 - T_{surf}^4) \tag{4}$$

where Q_{vol} is the volumetric heat source (W/m^3); a and b are the melt pool half width and half length; c is the melt pool depth; P_0 is the incident power; A is the liquid absorptance (= 0.35); x_0, y_0, and z_0 are the initial position of the heat source for each scan vector (dependent on the scan strategy); ρ (kg·m^{-3}), C_p (J·kg^{-1}·K^{-1}), and k (W·m^{-1}·K^{-1}) are the volumic mass, specific heat, and heat conductivity of the build material; ε is the emissivity (= 0.35); and σ is the Stefan-Boltzmann constant (= 5.67.10^{-8} W·m^{-2}·K^{-4}).

2.2 Computational domains and boundary conditions

A tetrahedral mesh strategy, with linear elements, is used on the whole computational domain, with mesh resolutions depending on the kind of model (GMLM

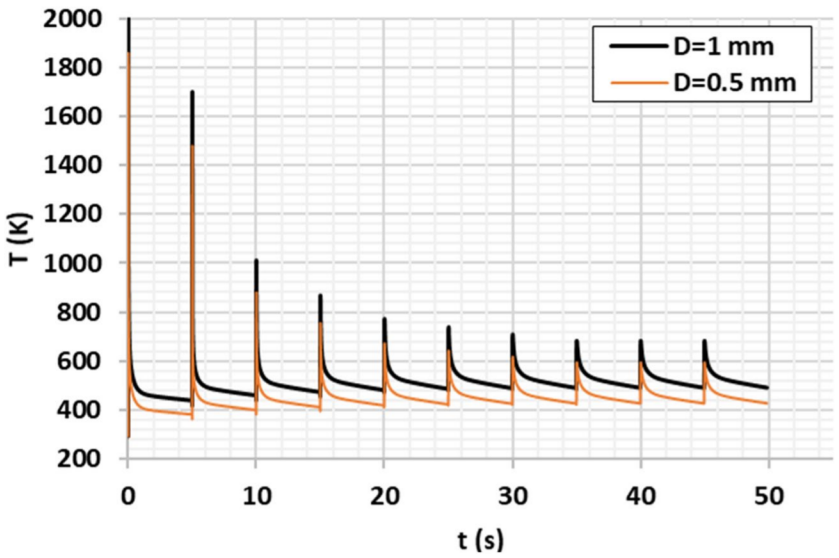

Fig. 9 Numerical determination of $T = f(t)$ profiles considered at $r/2$ of the struts (ten layers, 5-s time pause, 0.5 mm versus 1-mm struts, IO strategy)

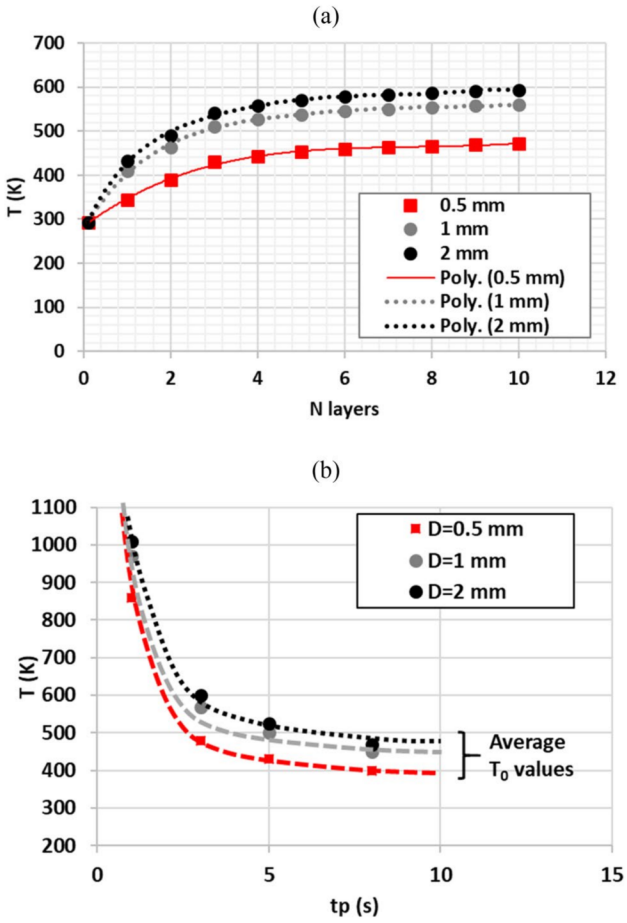

Fig. 10 Numerical determination of average strut's temperature (global model). **a** Influence of the number of layers (one to ten), 3-s time pause. **b** Influence of time pause (IO)

or HRSLM), as summarized in Table 3. Before defining such mesh conditions, a mesh optimization step was carried out considering highly refined conditions (down to 15 µm quadratic elements or 7 µm linear elements) for the HRSLM model. Adaptive remeshing was also used as a possible way to reduce calculation times and decrease local mesh size near the melt pool. However, no distinct modification was shown in terms of melt pool dimensions and thermal data near the solidification front (less than a 10% change in cooling rates and thermal gradients).

For the first GMLM model, which aims at calculating the average temperatures in the struts versus the number of built layers and time pauses, boundary conditions are considered as follows:

- Radiative and convective losses were imposed at the top surface of build layers during their activation stage and removed as soon as a new layer was activated.
- For this global model, convective losses were considered on all the external surfaces in contact with the powder. Due to the very low equivalent heat conductivity of the powder bed (k_{powder} (T) ~ 0.05 k_{solid} (T) following previous works by [10]), a $h = 25$ W·m^{-2}·K^{-1} convection loss coefficient was considered for the first model.

For both global and single-layer models, larger convective losses ($h = 300$ W·m^{-2}·K^{-1}) are imposed at the bottom surface of the computational domain, to represent the dissipation through the substrate. In the HRSLM model, the powder bed was considered part of the computational domain, to provide realistic interface losses. For each strut of strut radius, a 1-mm equivalent powder bed width was added around the strut (Fig. 2b), using a similar geometrical approach to [20]. For instance, the mesh domain of a 2-mm-diameter strut surrounded by the powder bed corresponds to a 4-mm diameter (2 mm + 2 × 1 mm), whereas the mesh domain of a 0.5-mm strut + powder bed has a 2.5-mm diameter (0.5 mm + 2 × 1 mm).

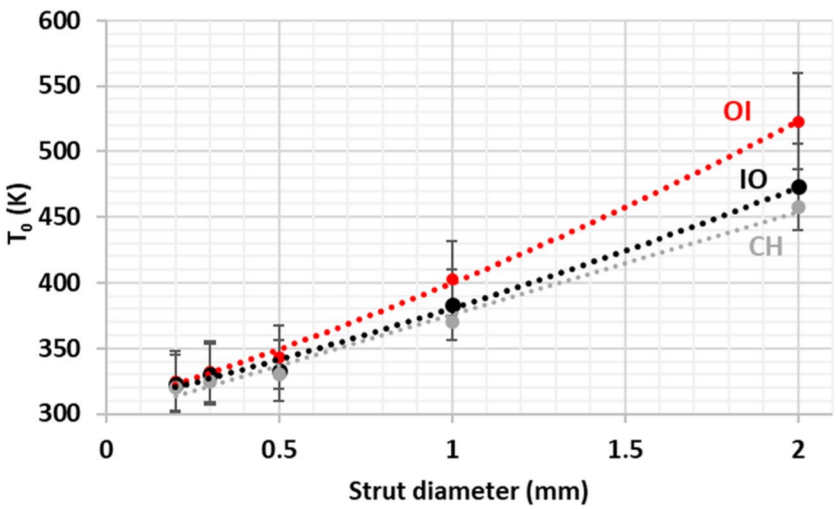

Fig. 11 Average temperature versus strut diameter for two contour strategies (IO, OI, and CH) and five strut diameters (simulated values, 10-s time pause)

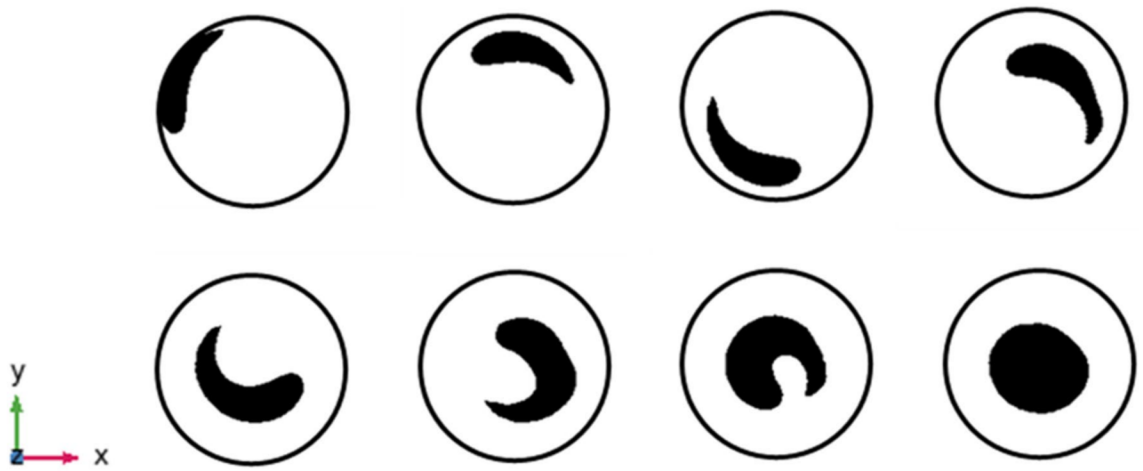

Fig. 12 Image analysis (after binarization) of numerical melt pools (top view, $D = 1$ mm, OI) at different scanning times. A maximum 30% ratio of the total area is molten

Fig. 13 Comparison between experimental and simulated melt pool areas versus lasing time: **a** for OI strategy and **b** for IO strategy (2-mm strut)

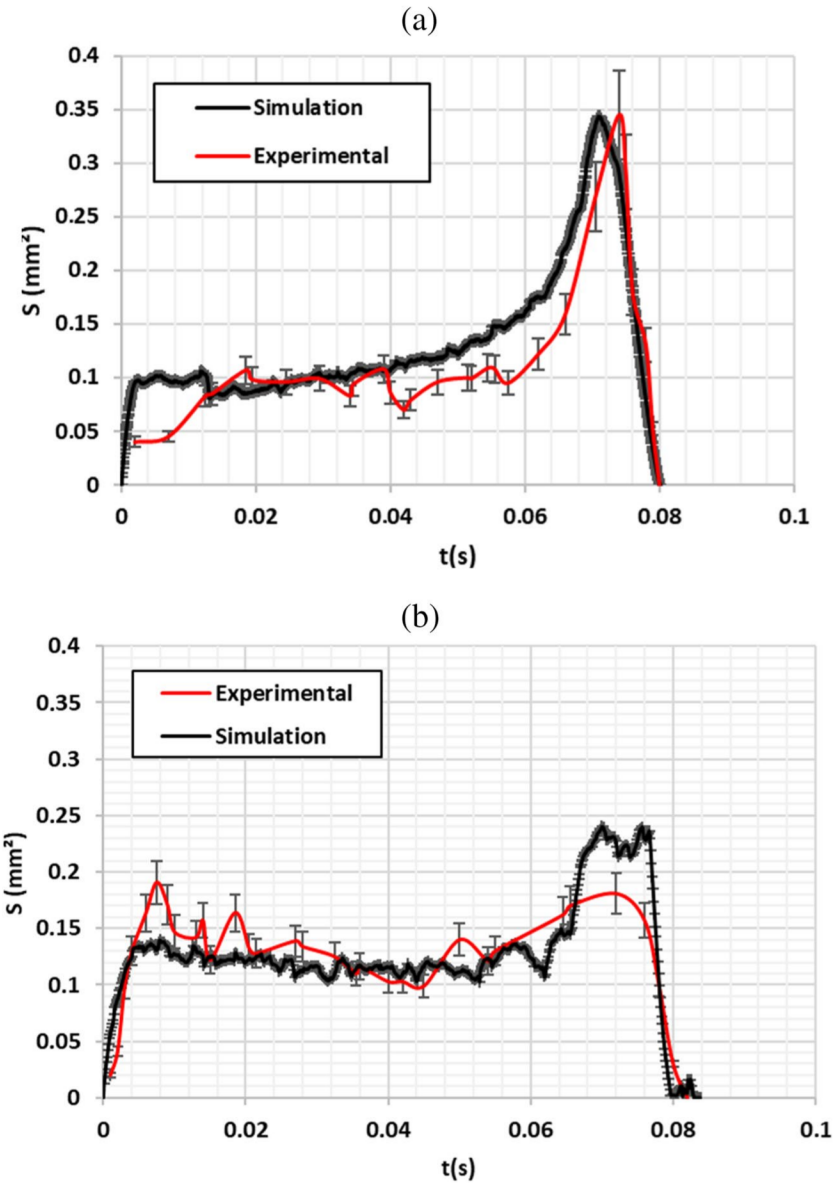

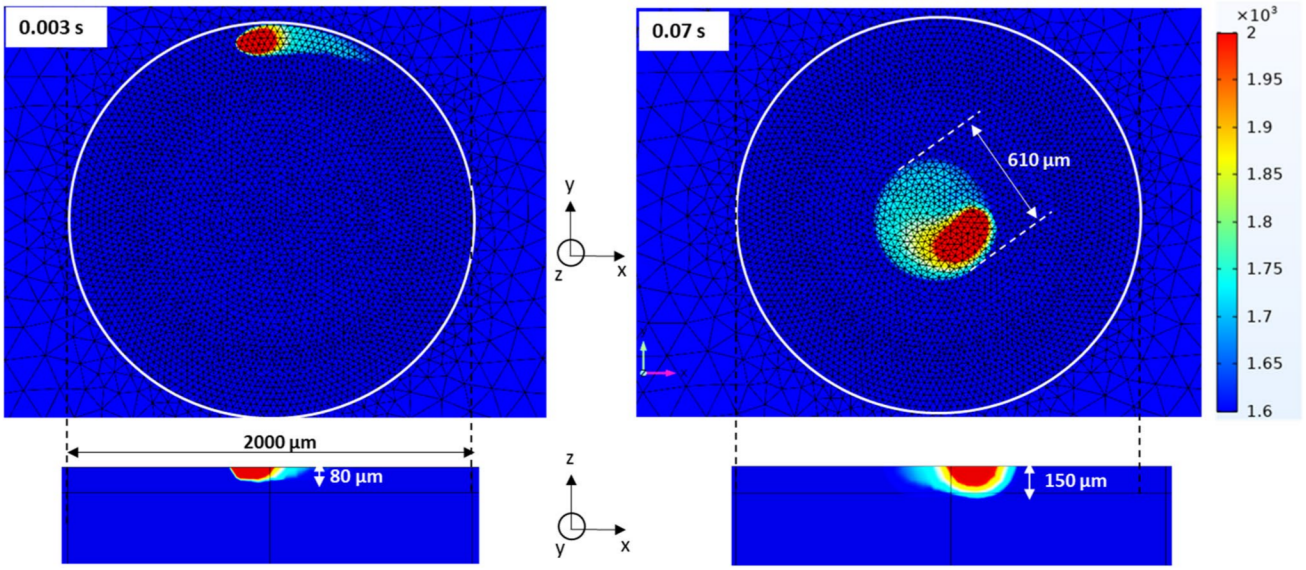

Fig. 14 Top and side view of simulated melt pools ($D = 2$ mm, OI contouring) at two build times (0.003 s and 0.07 s)

3 The L-PBF instrumented experiments

3.1 Experimental conditions

L-PBF tests were carried out in a home-made instrumented bench (Fig. 3), equipped with a 50-mm building platform, a 500-W fiber laser ($D_{las} = 70$ µm at $1/e^2$), and a controlled Ar atmosphere (< 500 ppm O_2). A constant layer height of 50 µm was used for all the tests. As indicated above (Sect. 2), three scan strategies, namely, pure contouring (IO and OI) or one contouring line + hatching lines (CH), were used for the builds (Fig. 4). For the smallest diameter (0.25 mm), only a single contouring line was used, as indicated in Table 4. The inter-scan line distance was 80 µm between contour circles and 120 µm between hatch lines, as recommended on Inconel 625 alloys by SLM Solutions GmbH. A high-speed imaging system (SA2 Photron) was used to capture instantaneous melt pool images on a 3 mm × 3 mm window (3 µm/pixel resolution) for various scan strategies and strut diameters. An illumination laser synchronized with the high-speed camera and operating at $\lambda = 810$ nm (Cavilux HF, Cavitar, Tampere, Finland) was used to improve melt pool detection. Recordings of L-PBF tests were made at 4000 fr/s frame rate, which allows capturing one image every 0.25 ms corresponding to a propagation distance of the melt pool of 125 µm at 0.5 m/s scan speed.

3.2 High-speed imaging

The high-speed imaging of strut surfaces (Fig. 5) during L-PBF is a rather complex and time-consuming task because melt pools are not correctly observed at each recording time, due to specular reflections of the Cavilux light on the liquid surface. However, interesting observations could be made:

- Larger melt pools are shown at the end of the layer fusion (Fig. 6) for the 2-mm diameter strut and the OI strategy. Such data, in terms of melt pool surfaces, are confronted with numerical simulations in Sect. 4. At the beginning of the OI contouring, elongated melt pools are shown whereas at the end of the laser path, a circular melt pool is formed at the central part of the strut. A similar result is observed for $D_0 = 1$ mm and an OI strategy.
- Larger differences between OI and IO strategies are observed for $D_0 = 2$ mm than for 1 mm, 0.5 mm, and 0.3 mm. For instance, in Fig. 6b (IO strategy), the melt pool at the end of melting (contour 10) is distinctly smaller than in Fig. 6a (OI strategy).
- For strut diameters of 0.5 mm, 0.3 mm, and 0.2 mm, a unique melt pool is formed on top of the struts during the contouring process (Fig. 7). This is an important point to notice because it should induce a different solidification mode.

4 Numerical results

4.1 Calibration of the Goldak source

Single L-PBF tracks were carried out experimentally and simulated numerically to calibrate the Goldak source and

estimate a, b, and c parameters (Fig. 8). The best fitting of the experimental track was obtained for $a = b = r_{las} = 35$ µm and $c = 70$ µm. As P_0, V_0, and D_0 were kept constant (125 W, 0.5 m/s, 70 µm) in all the work, such Goldak parameters were systematically used in all the simulations.

4.2 Influence of strut diameter, time pauses, and scan strategies on average struts' temperatures

The average strut's temperature decreases gradually with time pause but increases with the number of built layers as shown in Figs. 9, 10, and 11. To estimate the "stabilized" average temperatures, the following procedure has been used:

(1) From the $T = f(t)$ curves obtained for N layers (Fig. 9), we estimate average temperature data for a given time pause. Globally, for a $t_p = 3$ s time pause, temperatures are mostly stabilized after ten layers (Fig. 10a).
(2) For ten built layers, we consider the T_0 versus t_p dependence, which provides us with an estimation of a nearly stabilized T_0 value above $t_p = 10$ s (Fig. 10b).
(3) Average T_0 temperatures are reported versus strut diameters and OI, IO, and CH building strategy (Fig. 11).

Numerical results indicate that an increase in strut's diameter with a pure contour strategy or with a combined contour + hatching strategy increases the average reached

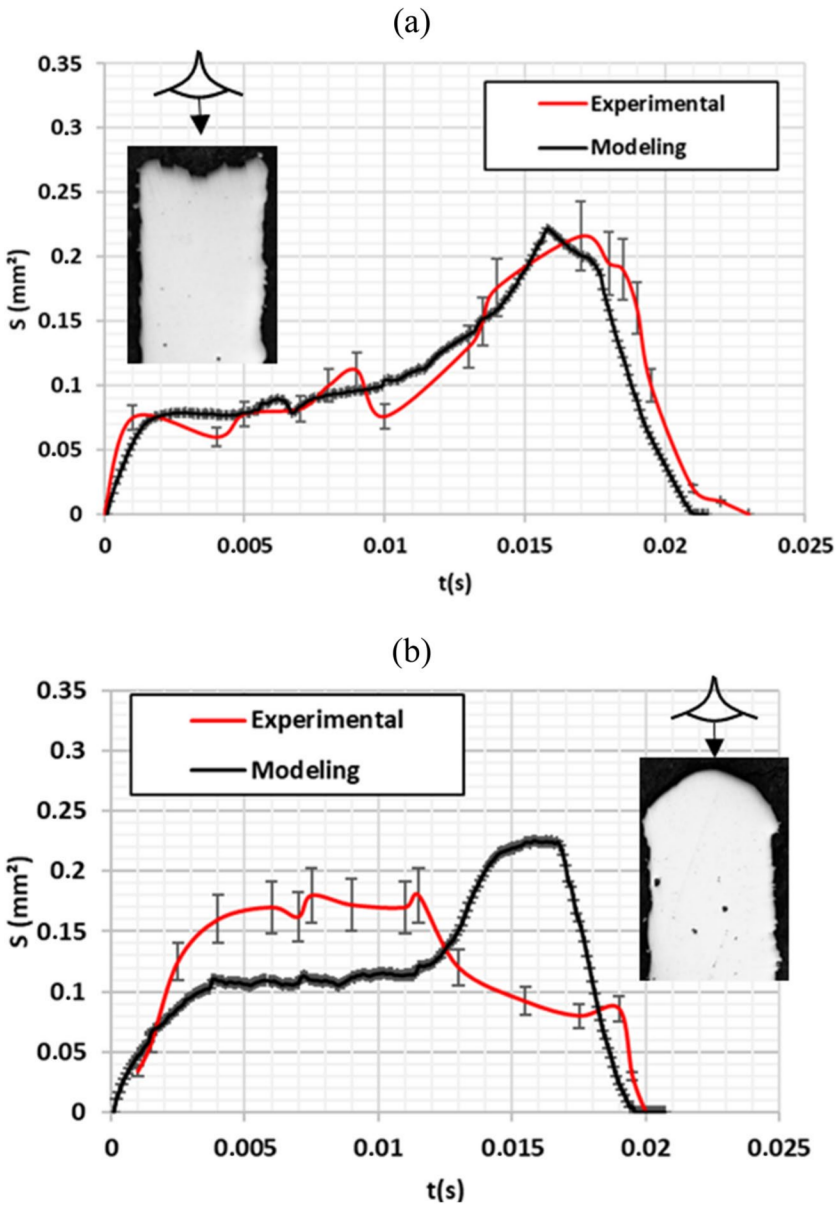

Fig. 15 Comparison between experimental and simulated melt pool areas versus lasing time: **a** for OI strategy and **b** for IO strategy (1-mm strut). Resulting macro cross-sections of struts are indicated, with a modification of concavity which can explain the observed difference in **b**

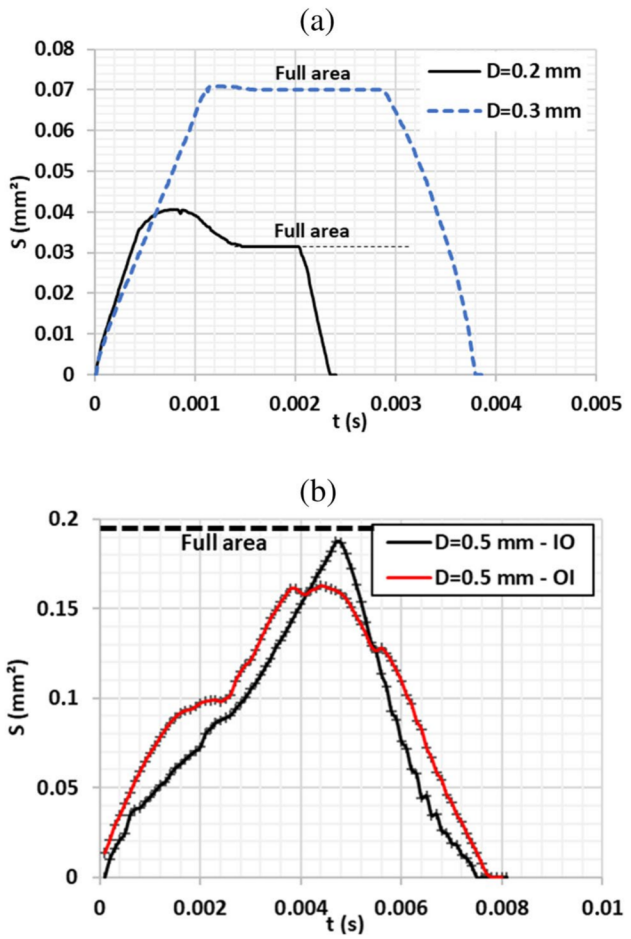

Fig. 16 Calculated melt pool areas versus lasing time: **a** for 0.2-mm and 0.3-mm struts and **b** for a 0.5-mm strut (contour strategy)

temperature T_0. The reason why larger struts are hotter is the number of scanned contours (11 for the 2-mm strut, 5 for the 1-mm strut, 2 for the 0.5 mm, and 1 for the 0.2 mm and 0.3 mm), which promotes larger heat accumulation, which is not counterbalanced by heat dissipation. For instance, average temperatures vary between 320 K (~ 50 °C) for the smaller diameter (0.2 mm) and 520 K (~ 240 °C) for the larger ($D = 2$ mm), with an OI contour strategy (Fig. 11).

The average temperature obtained for a CH strategy is also lower than for both IO and OI contouring conditions. Such temperatures are in the same order of magnitude as those evidenced by Promoppatum et al. [20] on a titanium alloy (60–120 °C).

Scan strategy also has a clear influence on L-PBF microstructures resulting from local thermal-cooling cycles experienced by each point of the built material. In the current work, two aspects were investigated: (1) the influence of scan direction (inside-out (IO) or outside–in (OI)) for a pure contouring strategy, (2) the comparison with a contour + hatching (CH) strategy (usual condition for large L-PBF parts). An example is shown in Fig. 11 where the OI strategy generates higher average temperatures than the IO mode. The heat accumulation due to the concentration of fusion isotherms at the central part of struts for the OI contour configuration may be a logical explanation for the observed results.

Finally, estimated T_0 temperatures for various strut diameters and scan strategies were considered as initial temperatures for the second HRSLM model.

4.3 Analysis of melt pool dimensions and local thermal data

Considering the initial strut temperature estimated in Sect. 4.2, the second model was applied to estimate more precisely the melt pool dimensions and thermal data: thermal gradient G (K·m^{-1}), solidification rate R (m·s^{-1}), and cooling rate $\dot{T} = V_c$ (K·s^{-1}) at the solidification front during the fusion of a single layer. The estimation of melt pool areas versus time was made automatically with an ImageJ© software routine applied to the total number of binarized images corresponding to the laser path (Fig. 12). The measurement of melt pool areas on high-speed images such as those shown in Fig. 5 was carried out manually on ImageJ©, due to the bad contrast between melt pool and surrounding matter.

Comparisons with experimental data were only possible for the larger strut's diameters (1 mm and 2 mm). The agreement between in situ imaging and modeling is globally very good and confirms a factor 2 to 3 increase of the melt pool surface S (mm^2) during the melting of each strut's surface (0.1 to 0.3 mm^2 in Fig. 13a), with a larger variation for the OI than for the IO strategy. Except for one case (1 mm, IO) which is discussed here below, the melt pool area tends to increase with time, due to the heat accumulation, and to the step-by-step heating of the metal at the nth track by the (n-1), (n-2) … tracks, favored by the short scan distance and cooling time between subsequent scan tracks.

At the end of the lasing step, the simulation confirms an increase in melt pool surface for the OI strategy (from 0.1 to 0.35 mm^2 for $D = 2$ mm (Fig. 13a)) and to a lesser degree for the IO strategy (Fig. 13b). This is due to the formation of a round, central, and large melt pool because of the decrease of scan contours with the OI strategy, which promotes local and central heat accumulation, as shown in Fig. 14. Such a phenomenon is also found for $D = 1$ mm (Fig. 15a) where approximately 30% of the strut's surface is molten at the end of lasing time.

Just like $D = 2$ mm experiments and simulations, melt pool areas analyzed on $D = 1$-mm struts exhibit fewer variations for the IO strategy. However, this configuration (1 mm, IO, Fig. 15b) is not well correlated to the numerical model. This difference might come from the

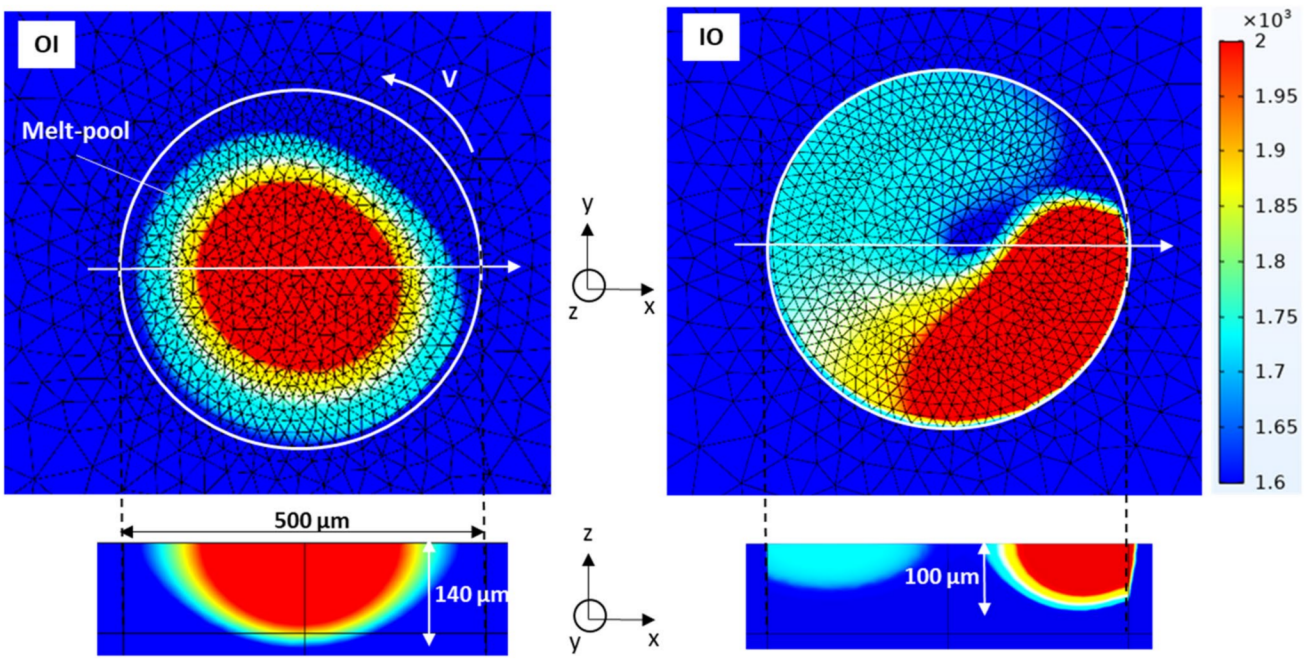

Fig. 17 Top and side view of melt pools ($D = 0.5$ mm, OI versus IO contouring strategy) at the end of lasing time (0.0045 s). For both strategies, the whole strut surface is almost fully melted

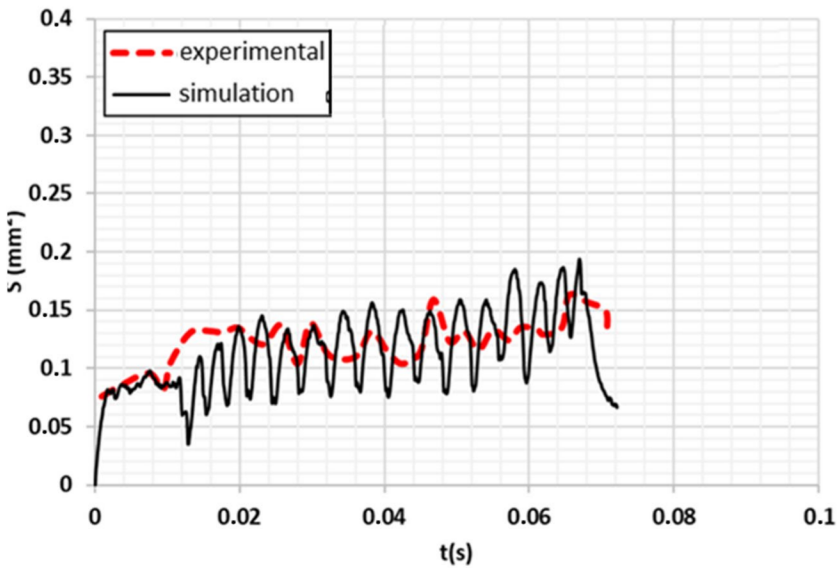

Fig. 18 Comparison between experimental and simulated melt pool areas for a CH (one contour + hatch) strategy ($D = 2$ mm)

deformation of the build surface, which creates a bump (Fig. 15b) and prevents an accurate measurement of real melt pool areas for this specific condition. In this specific case, one can assume that the geometrical curvature of the built surface is the main reason why experimental data underestimate (at the beginning of the scan) and overestimate (near the edges, at the end of the scan) real melt pool areas for the $D = 1$ mm, IO strategy.

For the smallest diameters of 0.2 mm, 0.3 mm, and 0.5 mm, simulations confirm that a unique melt pool forms on almost all the strut's surface (Fig. 16 and 17). On the 0.2-mm diameter (Fig. 16a), the molten surface slightly exceeds the total strut area, due to heat conduction in the surrounding equivalent powder bed. This "single droplet" effect, already evidenced with high-speed imaging (Fig. 7) and mentioned by Wang et al. [7], influences resulting microstructures, by promoting a vertical epitaxy between subsequent layers, and a more textured material as indicated in Sect. 5.

Finally, the use of a CH strategy, rather usual on larger L-PBF parts, induces periodic melt pool fluctuations on simulations (Fig. 18), with globally more constant melt

pool areas (0.1 to 0.15 mm^2) than with full contour strategies. The correlation with high-speed images is rather good, even if experimental images fail to highlight melt pool variations at the beginning and end of each scan track evidenced by FE modeling. This is possibly due to the lack of a sufficiently high number of clear experimental melt pool images, due to specular reflection of the Cavilux illumination.

4.4 Estimation of solidification conditions

Thermal simulations also allow estimating thermal parameters at the liquid/solid interface on each node of the model, and their evolution with the position inside struts. As widely indicated in the literature [16, 17], large cooling rates V_c ($K{\cdot}s^{-1}$) = G ($K{\cdot}m^{-1}$) * R ($m{\cdot}s^{-1}$) promote fine microstructures whereas large G/R favor columnar grains, which are dominant in L-PBF microstructures. In the current work, G and V_c thermal data are considered in the 1500–1600 K temperature range, corresponding roughly to the solidification interval, shifted down by 50 K to take into consideration undercooling effects at a high cooling rate. Local thermal data have been estimated at 60 µm below the surface, i.e., approximately at the half-depth of the melt pool, to consider solidification conditions for non-remolten zones.

Figures 19 and 20 show the distribution of cooling rate V_c ($K{\cdot}s^{-1}$) and thermal gradient G ($K{\cdot}m^{-1}$) along the O-y axis, i.e., along the diameter of the struts. Corresponding V_c values vary between -8.10^4 and $-4.2.10^5$ $K{\cdot}s^{-1}$ at 60 µm below the surface whereas local G values are comprised between $1.5.10^6$ and 8.10^6 $K{\cdot}m^{-1}$. Such cooling rates are approximately ten times lower than those estimated by Scipioni Bertoli et al. with an analytical Rosenthal model [16]. They are also two times lower than data obtained by Promoppatum et al. [20] in their modeling work. Other works by Ma et al. [15] also have evidenced larger cooling rates (2.10^6 to 5.10^6 $K{\cdot}s^{-1}$) with smooth particle hydrodynamic calculation on one L-PBF track whereas Olleak et al. [19] have mentioned lower cooling rates of $2–5.10^4$ $K{\cdot}s^{-1}$ (near the

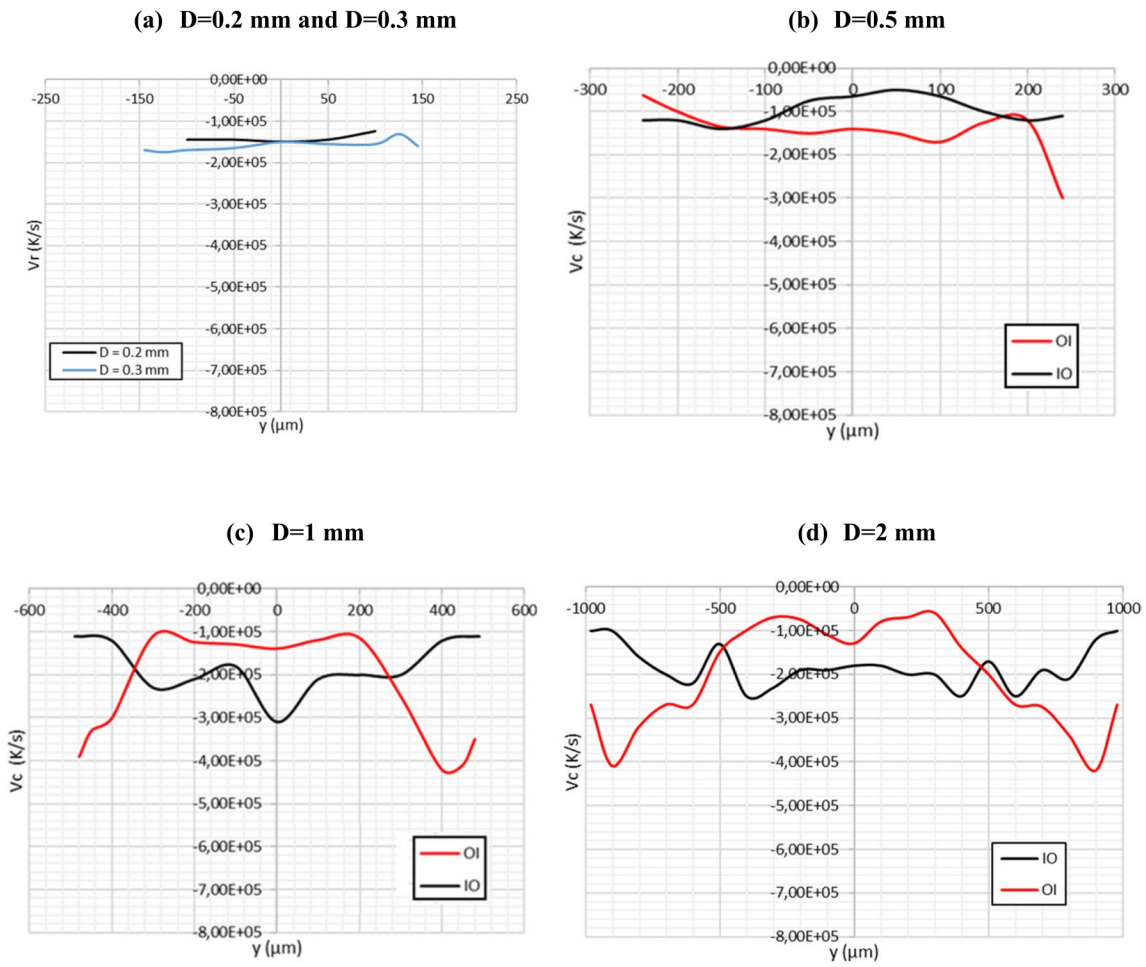

Fig. 19 Calculated local cooling rate V_c in the solidification interval: **a** 0.25-mm strut, **b** 0.5-mm strut, **c** 1-mm strut, and **d** 2-mm strut (IO or OI contour strategies)

transformation of titanium beta to titanium alpha temperature range (910–970 K).

Such differences in calculated cooling rates between our calculations and previous works may be explained by the following:

- The two to three times lower scan speeds used in the current work
- The fact that we considered such solidification conditions 60 µm below the surface, i.e., in areas non-remelted by subsequent layers, in the solidification interval ($T_{liq} - T_{sol}$) and not starting from the maximum melt pool temperature
- The preheating temperature T_0 considered in the current work which tends to lower cooling rates
- The mesh size near the solidification front which should be as small as possible

The distribution of V_c and G values along the (O, y) axis is logically not fully symmetrical because of the location of the starting point and its distance versus recorded data points. It also depends clearly on the strut size:

- For the smaller struts (0.2 mm, 0.3 mm, and 0.5 mm), G and V_c thermal parameters are almost stable along the strut diameter, due to the occurrence of a unique melt pool on all the strut's surface, which induces a near-planar solidification front (Fig. 7). This promotes a large gradient along z direction, a vertical epitaxy, and a < 001 > //BD (build direction) crystallographic texture.
- For the larger struts' diameters (1 mm and 2 mm), a larger scattering is shown on V_c and G values within the same sample, and a clear difference is obtained between OI and IO strategies. First, thermal data obtained with an OI strategy and the same strut diameter exhibit large differences between the core and the edge of the samples. For instance, -4.10^5 K/s is calculated on the external surface of the struts versus -1.10^5 K·s^{-1} in the central area (Fig. 19c, d), and a 7–8.10^6 K·m^{-1} gradient is shown near the surface of the strut versus a 2–2.5.10^6 K·m^{-1} gradient in the core (Fig. 20c, d). Comparatively, less V_c and G variations along the strut's diameter are shown with an IO strategy, with the larger values located in the core of the struts (Figs. 19 and 20).

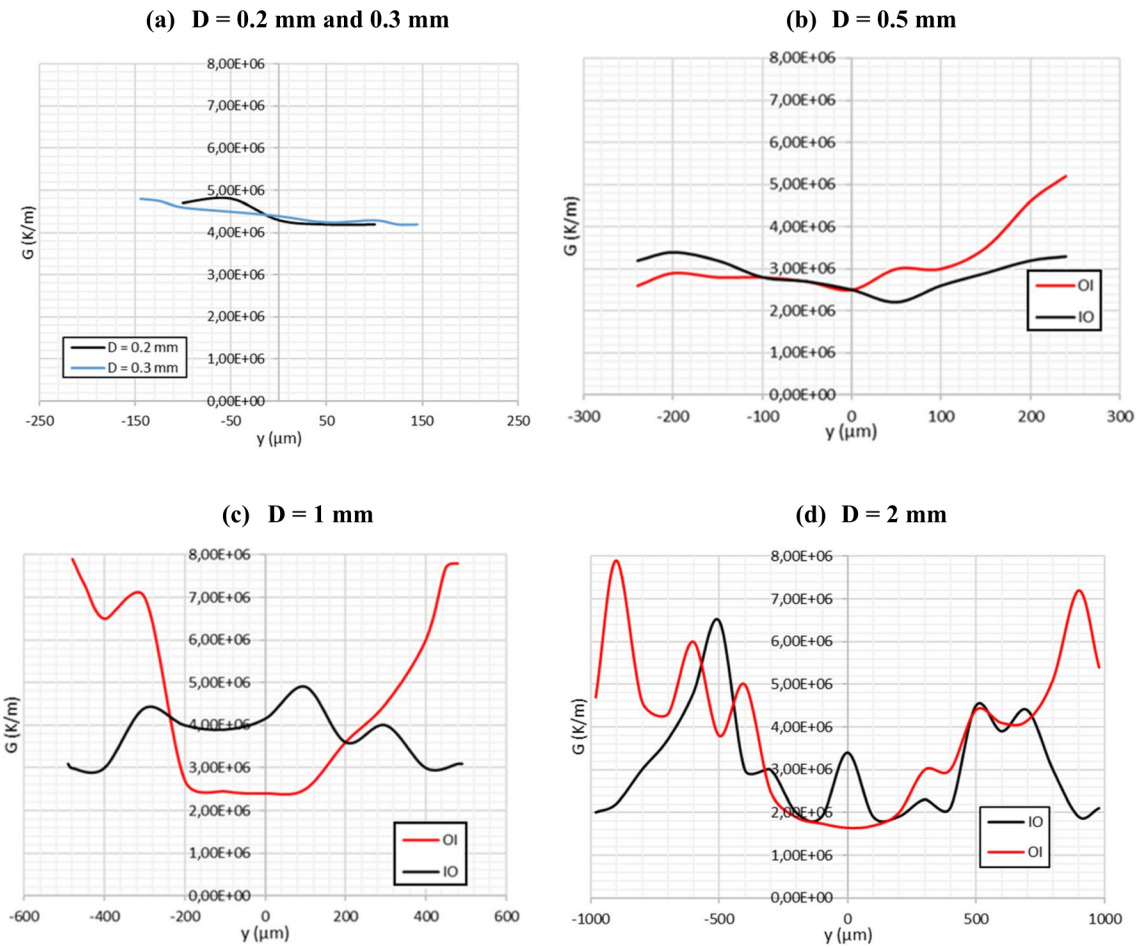

Fig. 20 Calculated thermal gradients for **a** 0.2-mm and 0.3-mm, **b** 0.5-mm, **c** 1-mm, and **d** 2-mm struts (IO or OI contour strategies)

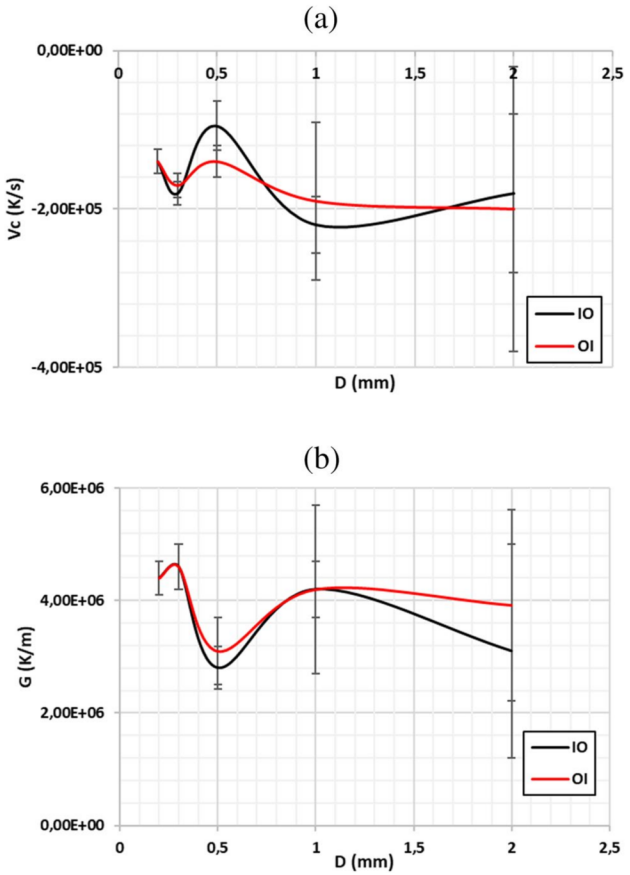

Fig. 21 **a** Average cooling rate V_c and **b** thermal gradient G for IO and OI contour strategies

A summary of V_c and G average data for a pure contouring strategy is presented in Fig. 21. Contrary to previous literature data on titanium [20], no clear increase in average cooling rates is shown for small diameters.

The local solidification conditions evidenced for a CH strategy (with contouring carried out first) also indicate a clear difference between the core and the surface of the struts where G and V_c values are 2 to 3 times higher than in the core (Fig. 22).

5 Discussion: microstructures versus solidification parameters

As indicated in Sect. 4.4, the selection and size of microstructures can be related directly to the more or less directional gradients G (K/m), to the fast cooling rates $G.R = \dot{T} = V_c$ (K·s^{-1}), and the G/R ratio (K·s·m^{-2}), all thermal parameters being considered near the solidification front. Locally, an increase in V_c values is expected to induce a refinement of solidification cells inside FCC grains. The combination of large grains and small solidification cells forms a hierarchical microstructure with directionally grown solidification cells, enriched with Nb and Mo as indicated by Marchese et al. [30]. Such solidification cells are separated by very low-angle grain boundaries (LAGB), which usually play a more significant strengthening role than larger high-angle grain boundaries (HAGB) according to Wang et al. on 316L steel [31]. As a reminder, on Ni-based superalloys such as Inconel 625, Li et al. [17] assumed a cell diameter $\delta = \beta.V_c^{-\lambda}$dependence between solidification cell diameter δ and cooling rate V_c, with β = average grain diameter ~ 50 µm and $\lambda = 0.33$.

In the current work, porosity rates were first estimated, based on optical micrographs carried out on longitudinal cross-sections, and coupled with image analysis using ImageJ software. Results (Fig. 23) indicate a decrease in porosity rate with struts' diameter and a maximum porosity of 0.45% in the smaller ($D = 0.2$ and $D = 0.3$ mm) struts. Results do not highlight any specific influence of build

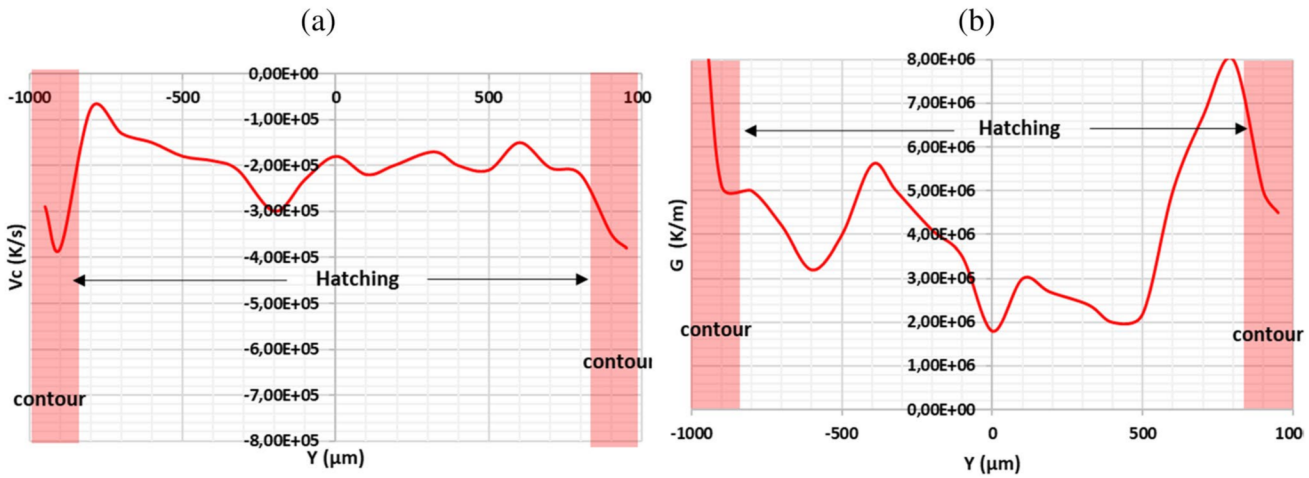

Fig. 22 **a** Local cooling rates V_c and **b** thermal gradients G for a CH strategy ($D = 2$ mm)

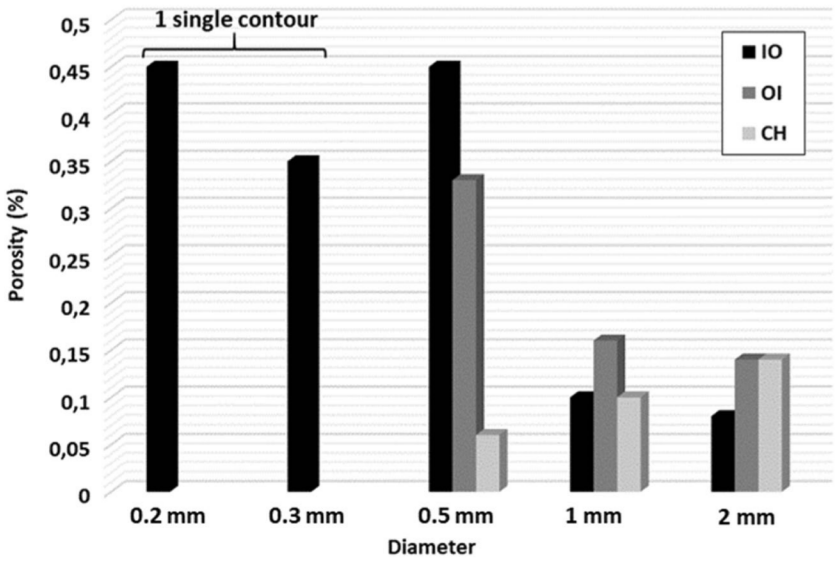

(a)

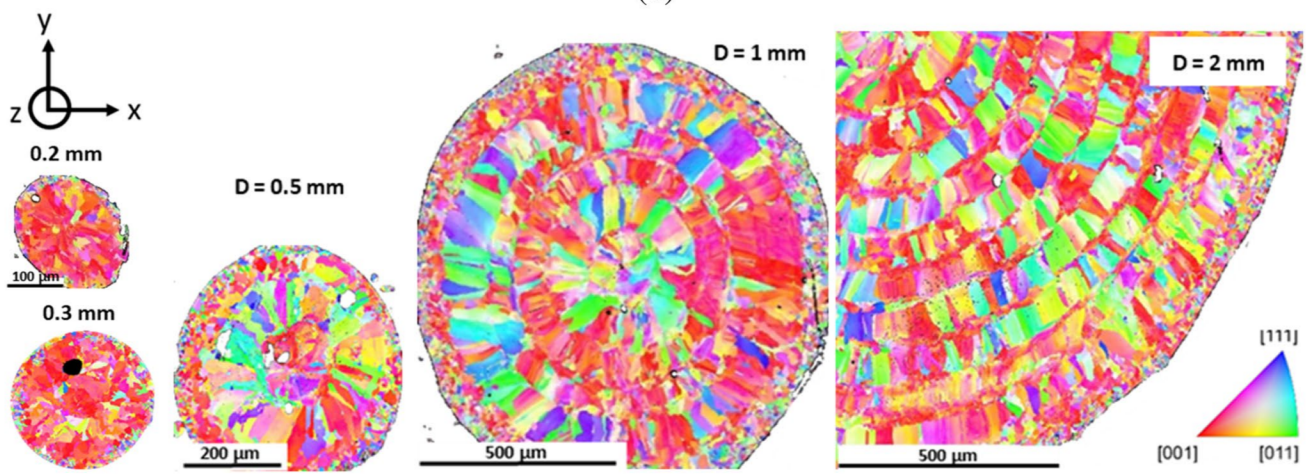

Fig. 23 Porosity rates on vertical struts

Fig. 24 EBSD analysis of struts. **a** Transverse (O, x, y) cross-sectional EBSD-IPF map concerning the z-axis for (from left to right) for a 0.2-mm strut, a 0.3-mm strut, a 0.5-mm strut, a 1-mm strut, and a 2-mm strut built (IO contouring strategy). **b** Corresponding pole figures (PF)

strategy on porosity generation. Comparatively, such porosity rates are relatively higher than those estimated by Wang et al. [7] on 316L vertical struts.

At the metallurgical grain scale, small struts generated by L-PBF with a contour strategy exhibit specific microstructures on cross-sections, mostly similar to a "dartboard" (Fig. 24):

- An outer ring with small (~ 10–20 µm) grains, with a near-constant width (~ 50–100 µm) whatever the strut diameter. When analyzed on a longitudinal section (Fig. 25a), such fine grains are columnar and slightly shifted (of ~ 10°) compared to the build direction (O, z). This very fine external crown, observed on all the struts cannot be explained by simulation data. For instance, simulated IO strategies mostly indicate higher cooling rates at the core of the 1-mm and 2-mm struts (Fig. 19c, d) whereas smaller struts exhibit nearly constant V_c values (Fig. 19a, b). Consequently, and as assumed already by [32], the surrounding powder grains (of 15–45 µm diameter) in contact with the struts could act as solidification germs to promote the nucleation and growth of small external grains having nearly the same diameter (10–20 µm).
- An inner part with columnar grains oriented parallel to the build direction, but with the occurrence of chevrons (Fig. 24a) resulting from lateral epitaxy between adjacent fusion tracks. Interestingly, the equivalent diameter of

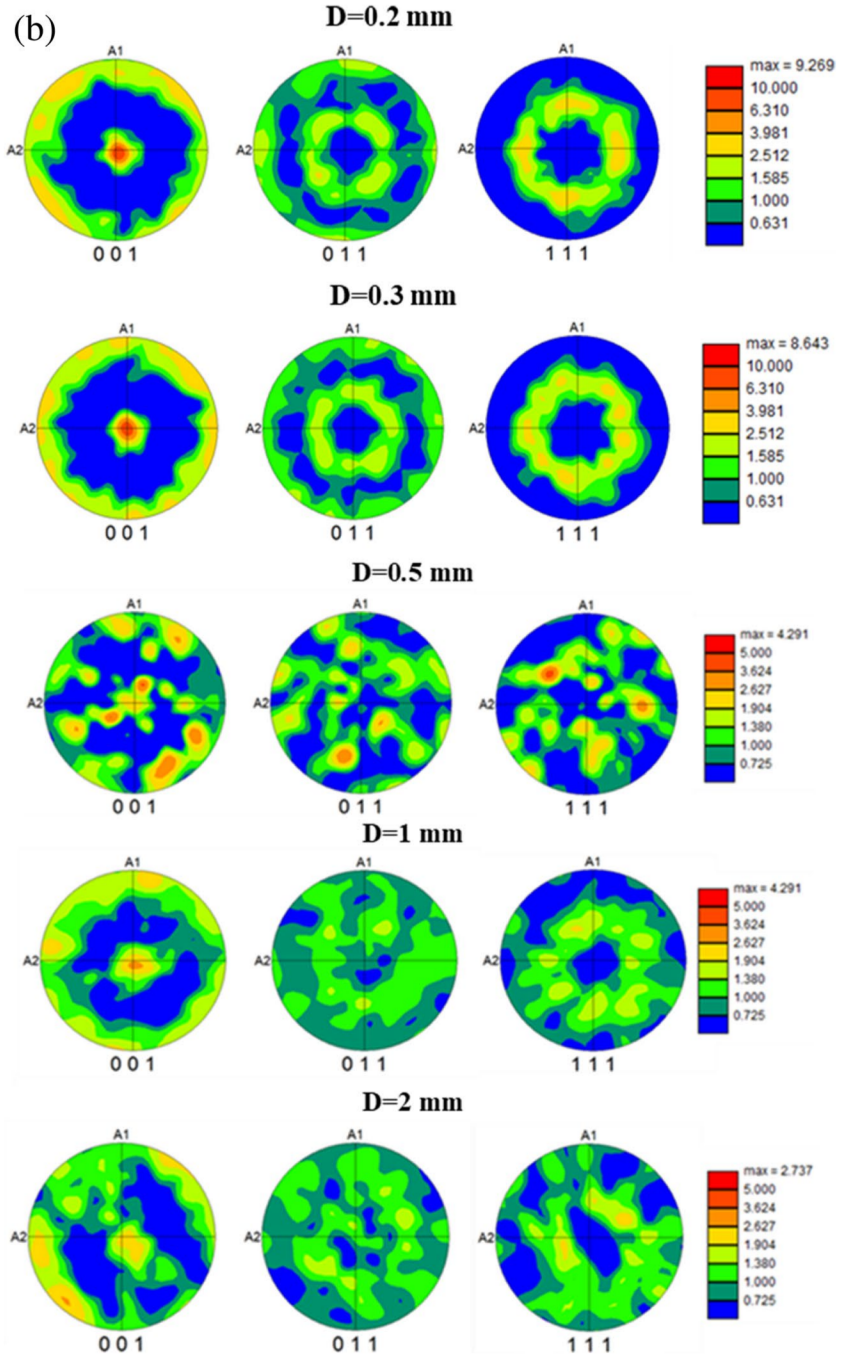

Fig. 24 (continued)

grains increases with strut size: from 40 µm ($D = 0.3$ mm) to 65 µm ($D = 0.5$ mm), 80 µm ($D = 1$ mm), and 90 µm for 2 mm, which disagrees with recent results on 316L [7]. This change in grain diameter is counterintuitive compared with the small increase in average cooling rate observed with the IO strategy for large strut's diameters (Fig. 21a). One possible explanation comes from the larger curvature radius of contour tracks for large struts, which limits the occurrence of disorientations.

A change in crystallographic texture with the strut's diameter is also observed with OI, IO, and CH strategies: the texture is clearly $<001>$ // BD for the smallest diameters (<0.5 mm) whereas the texture index decreases for larger diameters (1 mm and 2 mm) (Fig. 25b, c). This can be explained by the melt pool edge orientation versus BD. For large diameters, a 45° angle between the solidification front and BD mostly dominates, which orientates the $<100>$ direction of solidification cells with a 45° angle versus BD.

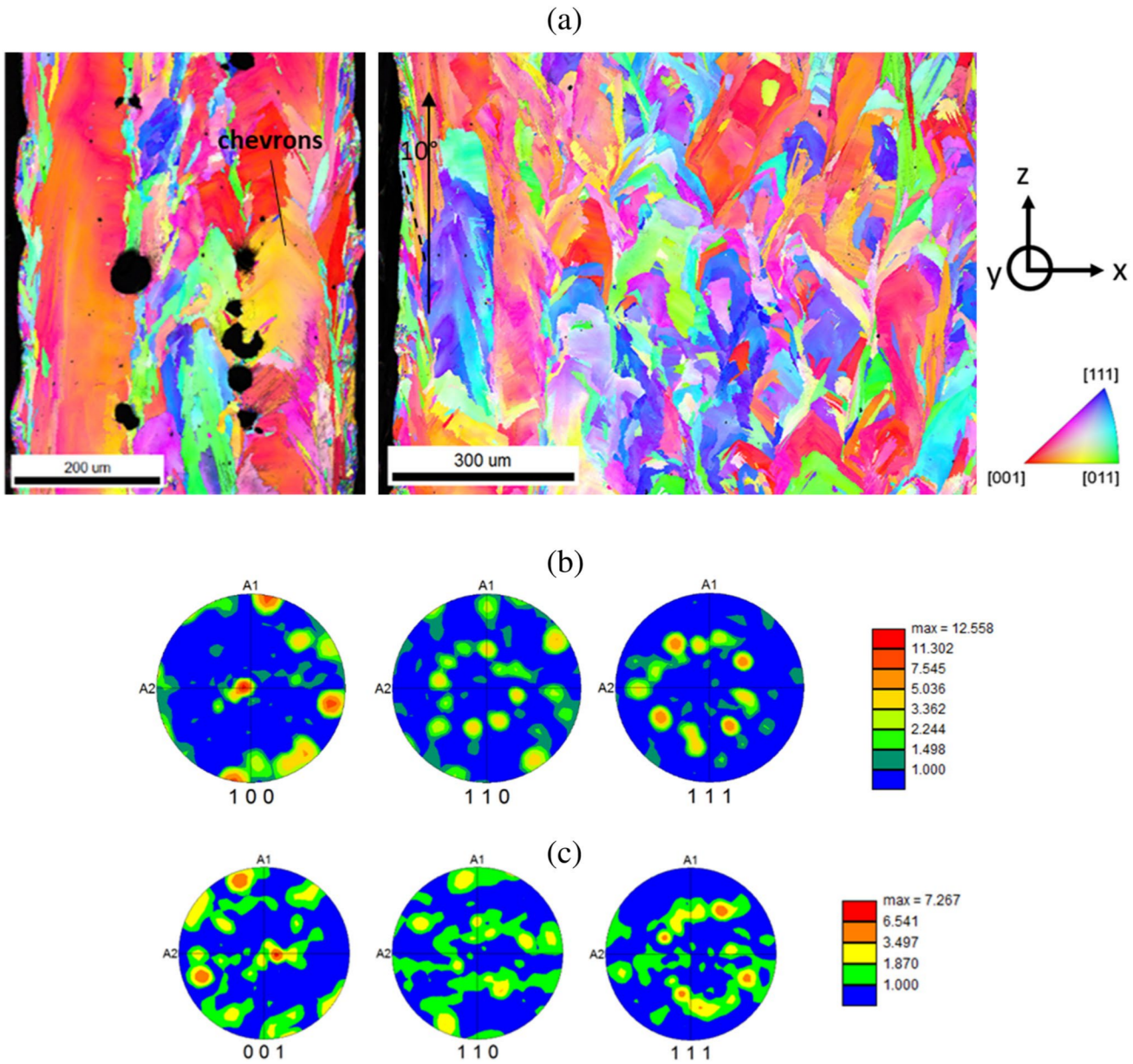

Fig. 25 Longitudinal (O, x, z) cross-sectional EBSD-IPF maps: **a** on a 0.5-mm strut (left) and a 2-mm strut (right) with a CH strategy (IPF map concerning the z-axis), **b** pole figure (PF) of the 0.3-mm cylinder with a < 100 > // BD texture, and **c** pole figure of the 2-mm cylinder with a less pronounced < 100 > //BD texture

This results in a mixture of < 100 > and < 110 > //BD texture (Fig. 26a), already explained in detail by Sofinowski et al. [33]. For the smallest strut's diameters (0.2 mm and 0.3 mm), a single melt pool is formed with a low curvature of the solidification front (Fig. 26b). This logically promotes an alignment of < 001 > direction // BD and explains the higher < 001 > texture evidenced with EBSD (Fig. 24).

The occurrence of a central melt pool generating a symmetrical solidification structure at the strut's central axis is confirmed by EBSD analysis of the last built layer with a contour OI strategy (Fig. 27), in agreement with numerical simulations (Fig. 14) and high-speed imaging (Fig. 6).

At the top of the last layer (Fig. 27), an equiaxed grain structure is also shown, which indicates higher solidification speeds and lower thermal gradients. However, this equiaxed zone is only detectable on the last built area, not remelted by subsequent layers.

The occurrence of an equiaxed zone on the upper part of the fusion zones can be explained by considering a columnar to equiaxed model like Hunt's criterion [34], already used by Hu et al. [35] on Inconel 625.

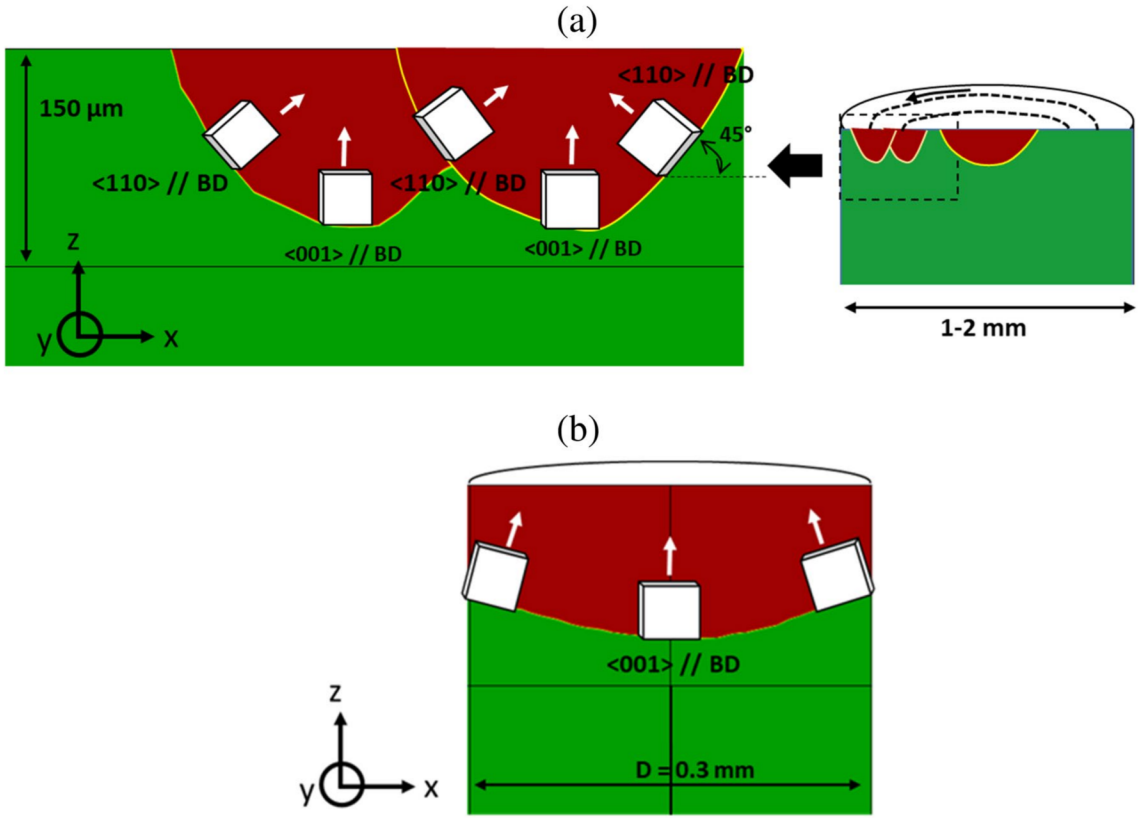

Fig. 26 Selection of crystal orientation from the calculated melt pool shapes (case of a contour strategy). **a** For 1 mm- and 2-mm diameters: the < 110 > growth // BD is dominant. **b** On a 0.3-mm diameter: the < 001 > orientation //BD dominates due to the low curvature of solidus isotherm when the melt pool occupies the whole strut's diameter

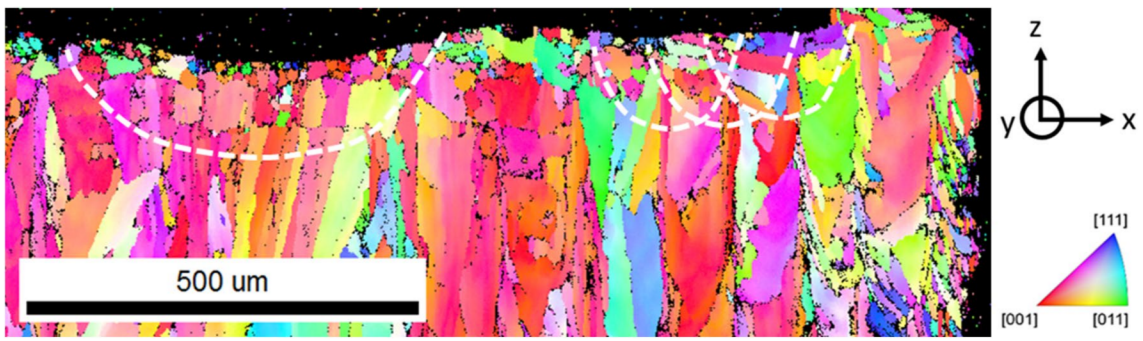

Fig. 27 Cross-sectional EBSD-IPF map of the top surface of a 2-mm strut concerning the *z*-axis (OI strategy). A large fusion zone is evidenced in the middle of the strut, with a < 001 > texture // (*O*, *z*). Equiaxed grains are also visible at the top of the fusion zones

This model (Eq. 5) considers a transition from columnar to equiaxed grains when the volume fraction of equiaxed grains in the undercooled zone (ahead of the Liq/Sol interface) is large enough to stop the columnar front growth. The use of Hunt's model on Inconel 625 (Fig. 28), combined with our numerical estimations of *R* and *G* well, confirms that the microstructure is mostly columnar, except on the very top of melt pools for which an equiaxed solidification is predicted.

$$G = \frac{1}{R}\sqrt[3]{\frac{N_g}{f_{eq}}\cdot\frac{4\pi}{81}}\cdot\left(\left(\frac{R}{A}\right)^{3/2} - \Delta T^3\right) \quad (5)$$

where N_g is the density of germs (10^{12} m^{-3}), ΔT is the undercooling (2 K), f_{eq} is the fraction of equiaxed grains, A is the constant (10^{-5}), and R is the solidification rate (m·s^{-1}).

Lastly, the SEM analysis of slightly disoriented (< 1° angle) sub-grain solidification cells indicates the following:

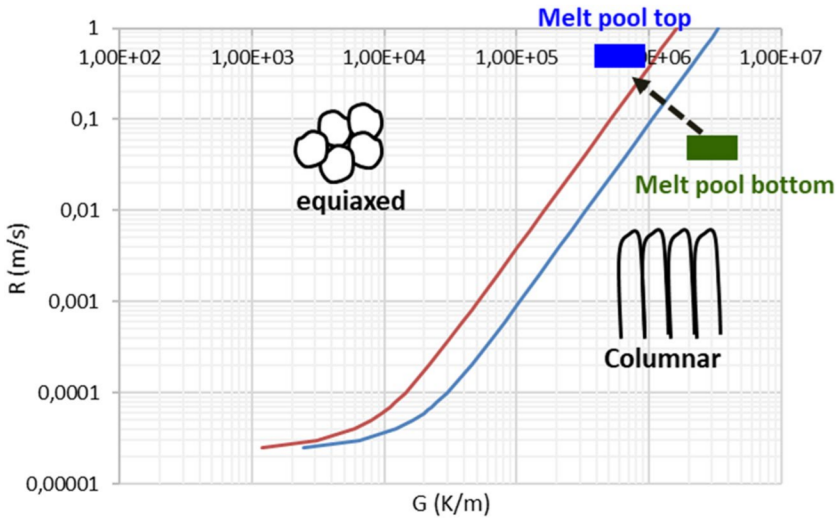

Fig. 28 Solidification speed versus thermal gradient diagram for Inconel 625, based upon Hunt's criterion [35]

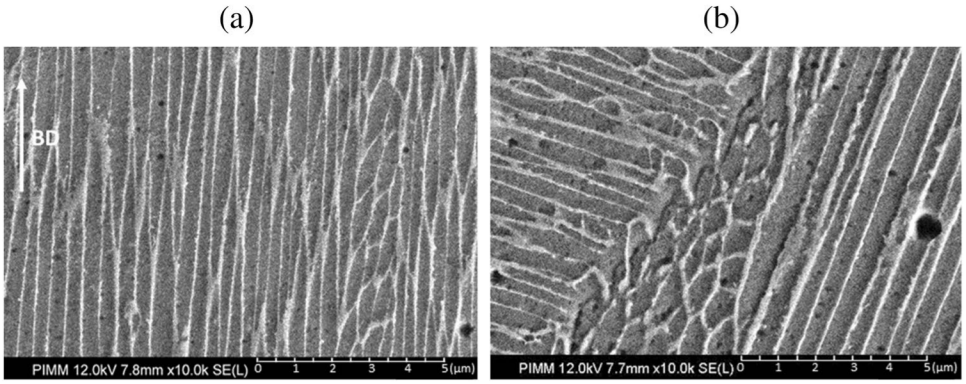

Fig. 29 SEM analysis of solidification cells (2-mm diameter, contour OI). **a** Near the strut's border (average inter-cell distance $\delta = 0.5\ \mu m \pm 0.2\ \mu m$). **b** In the middle of the strut (average inter-cell distance $\delta = 0.9 \pm 0.3\ \mu m$). Larger cells are observed in the middle of the struts

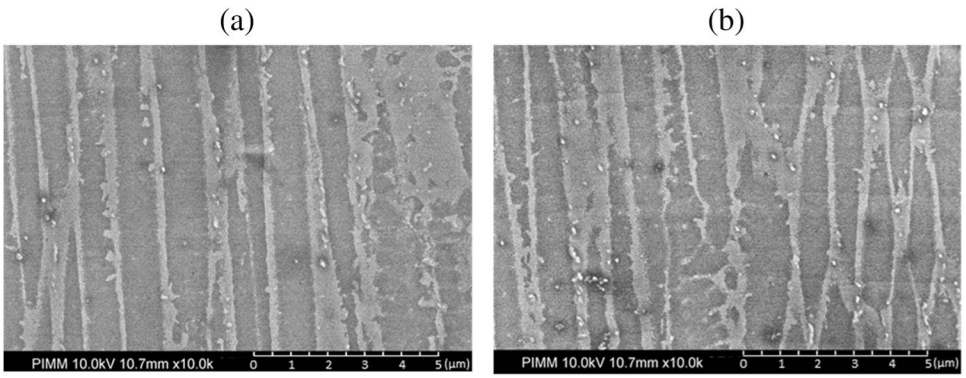

Fig. 30 SEM analysis of solidification cells on 0.25-mm struts (average inter-cell distance $1.6 \pm 0.4\ \mu m$): **a** near strut border and **b** in the middle of the strut

(1) Contrary to previously published works on 316L [7] [16] and Inconel 625 [17], there is a rather large scatter on solidification cell width δ which hinders precise estimations.
(2) A large proportion of cells is oriented towards the build direction BD (Fig. 29).

(2) Cell dimensions tend to decrease with the strut's diameter (between 1.6 and 0.5 µm) following the results by Wang et al. [7] on 316L (Fig. 29, Fig. 30). For the small diameter, the increase of cell dimensions is associated with larger inter-cellular spaces enriched with Nb and Cr (Fig. 29b).

(3) For the larger struts (1 mm and 2 mm), cells are smaller near the outside area, than at the strut's central part (Fig. 29), in full agreement with the simulation results of cooling rates (Fig. 19c, d).

Considering the $\delta = 50.\ V_c^{-0.33}$ formulation already presented by Li et al. [17], cooling rates V_c in the $-3.10^4\ K{\cdot}s^{-1}$ (small struts)/$-3.10^5\ K{\cdot}s^{-1}$ (large struts) range were estimated from the analysis of the cell's width. Such estimated

values are rather close to numerically determined values (Fig. 21).

However, the average numerical V_c values (Fig. 21a) do not vary significantly and regularly with strut diameters (values are always comprised between -1.10^5 and $-2.1.10^5$ K·s^{-1}) and do not highlight a significant decrease of V_c for small struts. For such a factor of two in cooling rates, the change in cell size should not exceed + 20% considering δ -V_c analytical dependence.

Therefore, the numerical model fails to provide a good estimation of cell dimensions versus strut's diameters. Interestingly, it also has to be mentioned that, considering the strut's cooling over longer durations (~ 1 s), lower cooling rates are obtained with large struts in agreement with [20].

On the other hand, the numerical model provides a satisfactory insight into the V_c and G gradients along the strut's diameter, which are higher near the strut's border, especially for large struts (Figs. 19c, d and 20c, d), and for the OI contouring strategy. Such a difference is confirmed by the observed cell dimensions δ (Fig. 29).

Finally, the numerical model mostly helps understanding microstructures at the solidification cell scale and their dependence on build strategy and strut diameter. It also confirms a clear reduction of V_c and G variations along the strut diameter for strut diameters below 0.5 mm, which explains why solidification cells are nearly constant in size for small diameters (Fig. 30). Such constant V_c and G values are mostly due to the formation of a single circular melt pool fulfilling the whole struts' top surface (Fig. 17) for $D = 0.2$, 0.3, and 0.5 mm.

Finally, the advantages of the current modeling are as follows: (1) to provide a realistic overview of laser-induced melt pools by considering all the L-PBF thermal history, and not a single L-PBF track, and by validating the model with experimental data, (2) to limit computational times by a two-step approach (GMLM and HRSLM models), and (3) to ensure a satisfactory prediction of the influence of build strategy and strut diameters. Its limitations come from the pure solid thermal approach, which did not consider fluid flow (Marangoni) as an important contributor to melt pool geometries and resulting microstructures. However, this assumption, and the use of an equivalent heat source, can be justified because the same (P, V) values were used for all the calculations. Extending the model to new (P, V) conditions would require further calibration of the Goldak heat source.

6 Conclusion

The present work includes the development of a simplified 3D thermal model for additively manufactured struts and the confrontation of numerical calculations with high-speed melt pool (MP) monitoring. The main objective was to address the influence of strut diameter (0.25 mm to 2 mm) and L-PBF scan strategy on solidification conditions and resulting microstructures on an Inconel 625 alloy through the analysis of melt pool areas.

First, a two-scale thermal model was implemented and calibrated, to calculate (1) average build temperatures (step 1) and (2) melt pool shapes and solidification conditions (step 2). Second, an open-architecture L-PBF set-up was used to monitor melt pools over time and compare experimental melt pool areas with numerical calculations. Third, struts' microstructures were analyzed using EBSD and SEM techniques.

The main results can be summarized as follows:

- Experimental and numerical data confirm that below 0.5-mm diameter, and whatever the scan strategy, a unique melt pool forms at the top of each layer, which solidifies with a strong epitaxy with previously built layers and a < 001 > // BD crystal orientation.
- Above 0.5 mm, and especially for $D = 1$ mm and $D = 2$ mm, the influence of scan strategy becomes dominant, and large differences are shown between the IO and OI modes in terms of local cooling rates V_c (K·s^{-1}).
- The OI strategy induces larger cooling rates and thermal gradients at the surface of struts, especially for the large diameters, in full agreement with the size of solidification cells.
- Surprisingly, the calculated average cooling rates (around -2.10^5 K·s^{-1}) and thermal gradients (around 4.10^6 K·m^{-1}) near the solidification front do not vary very significantly concerning the struts' diameter and scan strategy.

Finally, even if it fails to fully connect solidification cell width with local cooling rate, such a model, combined with high-speed melt pool monitoring and metallurgical analysis, provides an original insight into the influence of size and strategy effects on melt pools and induced microstructures in additively manufactured vertical struts. It also helps selecting adequate build conditions or strut diameters for ensuring satisfactory microstructures in supporting structures or structure lattices.

Future work should concern the experimental and numerical analysis of the influence of build angle for inclined struts, to fully consider the constitutive parts of lattice structures.

Acknowledgements The current work has been performed in the frame of an 80PRIME Ph.D. grant by French CNRS.

Author contribution All authors contributed to the study's conception and design and the writing of the paper.

The global supervision of the work was carried out by T. Baudin, AL. Helbert, Z. Hamouche, and P. Peyre.

Modeling work was carried out by P. Peyre, M. Dal, and J. Daligault.

L-PBF tests and melt pool monitoring were carried out by J. Rodrigues, P. Peyre, and F. Coste.

Microstructure investigations (experiments + discussion) were performed by J. Rodrigues, P. Peyre, Z. Hamouche, T. Baudin, and AL. Helbert.

Funding This work was granted by French CNRS in the frame of the 80PRIME call.

Data availability Data are available for further investigations.

Code availability Not applicable.

Declarations

Ethics approval Not applicable.

Consent to participate All authors consent to participate in the presented work.

Consent for publication All authors have read and approved the final manuscript.

Competing interests The authors declare no competing interests.

References

1. Herzog D, Scholl C, Klemp C, Maiwald M-I (2022) Additive manufacturing of large-scale aerospace engine parts. In: Towards sustainable aviation summit (TSAS 2022). Toulouse (Fr)
2. Tyagi SA, Manjaiah M (2023) Additive manufacturing of titanium-based lattice structures for medical applications – a review. Bioprinting 30:e00267. https://doi.org/10.1016/j.bprint.2023.e00267
3. Scalzo F, Totis G, Vaglio E, Sortino M (2021) Experimental study on the high-damping properties of metallic lattice structures obtained from SLM. Precis Eng 71:63–77. https://doi.org/10.1016/j.precisioneng.2021.02.010
4. Dell'Isola F, Seppecher P, Spagnuolo M et al (2019) Advances in pantographic structures: design, manufacturing, models, experiments and image analyses. Contin Mech Thermodyn 31:1231–1282. https://doi.org/10.1007/s00161-019-00806-x
5. Sombatmai A, Uthaisangsuk V, Wongwises S, Promoppatum P (2021) Multiscale investigation of the influence of geometrical imperfections, porosity, and size-dependent features on the mechanical behavior of additively manufactured Ti-6Al-4V lattice struts. Mater Des 209:109985. https://doi.org/10.1016/j.matdes.2021.109985
6. Barba D, Alabort C, Tang YT et al (2020) On the size and orientation effect in additive manufactured Ti-6Al-4V. Mater Des 186:108235. https://doi.org/10.1016/j.matdes.2019.108235
7. Wang X, Muñiz-Lerma JA, Sánchez-Mata O et al (2018) Microstructure and mechanical properties of stainless steel 316L vertical struts manufactured by laser powder bed fusion process. Mater Sci Eng A 736:27–40. https://doi.org/10.1016/j.msea.2018.08.069
8. Britt C, Montgomery CJ, Brand MJ et al (2021) Effect of processing parameters and strut dimensions on the microstructures and hardness of stainless steel 316L lattice-emulating structures made by powder bed fusion. Addit Manuf 40:101943. https://doi.org/10.1016/j.addma.2021.101943
9. Soundararajan B, Sofia D, Barletta D, Poletto M (2021) Review on modeling techniques for powder bed fusion processes based on physical principles. Addit Manuf 47:102336. https://doi.org/10.1016/j.addma.2021.102336
10. Mayi YA, Dal M, Peyre P et al (2023) Physical mechanisms of conduction-to-keyhole transition in laser welding and additive manufacturing processes. Opt Laser Technol 158:108811. https://doi.org/10.1016/j.optlastec.2022.108811
11. Khairallah SA, Anderson AT, Rubenchik A, King WE (2016) Laser powder-bed fusion additive manufacturing: physics of complex melt flow and formation mechanisms of pores, spatter, and denudation zones. Acta Mater 108:36–45. https://doi.org/10.1016/j.actamat.2016.02.014
12. Afazov S, Roberts A, Wright L et al (2022) Metal powder bed fusion process chains: an overview of modeling techniques. Prog Addit Manuf 7:289–314. https://doi.org/10.1007/s40964-021-00230-1
13. Xue C, Blanc N, Soulié F et al (2022) Structure and texture simulations in fusion welding processes – comparison with experimental data. Materialia 21:101305. https://doi.org/10.1016/j.mtla.2021.101305
14. Camus T, Gandin C-A, Guillemot G (2021) Modelling of microstructures development in laser powder bed fusion process - application on an IN718 nickel-base superalloy, – EUROMAT 2021. https://doi.org/10.1088/1757-899X/1274/1/012019
15. Ma J, Niu X, Zhou Y et al (2023) Simulation of solidification microstructure evolution of 316L stainless steel fabricated by selective laser melting using a coupled model of smooth particle hydrodynamics and cellular automata. J Mater Res Technol 27:600–616. https://doi.org/10.1016/j.jmrt.2023.09.296
16. Scipioni Bertoli U, MacDonald BE, Schoenung JM (2019) Stability of cellular microstructure in laser powder bed fusion of 316L stainless steel. Mater Sci Eng A 739:109–117. https://doi.org/10.1016/j.msea.2018.10.051
17. Li S, Wei Q, Shi Y et al (2015) Microstructure characteristics of Inconel 625 superalloy manufactured by selective laser melting. J Mater Sci Technol 31:946–952. https://doi.org/10.1016/j.jmst.2014.09.020
18. Olleak A, Dugast F, Bharadwaj P et al (2022) Enabling part-scale scanwise process simulation for predicting melt pool variation in LPBF by combining GPU-based matrix-free FEM and adaptive re-meshing. Addit Manuf Lett 3:100051. https://doi.org/10.1016/j.addlet.2022.100051
19. Olleak A, Adcock E, Hinnebusch S et al (2024) Understanding the role of geometry and interlayer cooling time on microstructure variations in LPBF Ti6Al4V through part-scale scan-resolved thermal modeling. Addit Manuf Lett 9:100197. https://doi.org/10.1016/j.addlet.2024.100197
20. Promoppatum P, Taprachareon K, Chayasombat B, Tanprayoon D (2022) Understanding size-dependent thermal, microstructural, mechanical behaviors of additively manufactured Ti-6Al-4V from experiments and thermo-metallurgical simulation. J Manuf Process 75:1162–1174. https://doi.org/10.1016/j.jmapro.2022.01.068
21. Zhao C, Fezzaa K, Cunningham RW et al (2017) Real-time monitoring of laser powder bed fusion process using high-speed X-ray imaging and diffraction. Sci Rep 7:3602. https://doi.org/10.1038/s41598-017-03761-2
22. Zhang H, Vallabh CKP, Zhao X (2022) Registration and fusion of large-scale melt pool temperature and morphology monitoring data demonstrated for surface topography prediction in LPBF. Addit Manuf 58:103075. https://doi.org/10.1016/j.addma.2022.103075
23. Mitchell JA, Ivanoff TA, Dagel D et al (2020) Linking pyrometry to porosity in additively manufactured metals. Addit Manuf 31:100946. https://doi.org/10.1016/j.addma.2019.100946
24. Gunenthiram V, Peyre P, Schneider M et al (2018) Experimental analysis of spatter generation and melt-pool behavior during the powder bed laser beam melting process. J Mater Process Technol 251:376–386. https://doi.org/10.1016/j.jmatprotec.2017.08.012
25. Bidare P, Maier RRJ, Beck RJ et al (2017) An open-architecture metal powder bed fusion system for in-situ process measurements. Addit Manuf 16:177–185. https://doi.org/10.1016/j.addma.2017.06.007

26. Leary M, Mazur M, Williams H et al (2018) Inconel 625 lattice structures manufactured by selective laser melting (SLM): mechanical properties, deformation, and failure modes. Mater Des 157:179–199. https://doi.org/10.1016/j.matdes.2018.06.010
27. Moslemi N, Abdi B, Gohari S et al (2022) Influence of welding sequences on induced residual stress and distortion in pipes. Constr Build Mater 342:127995. https://doi.org/10.1016/j.conbuildmat.2022.127995
28. Mills KC (2002) Recommended values of thermo-physical properties for selected commercial alloys. Woodhead Publishing, ASM International
29. Baumard A, Ayrault D, Fandeur O et al (2021) Numerical prediction of grain structure formation during laser powder bed fusion of 316 L stainless steel. Mater Des 199:109434. https://doi.org/10.1016/j.matdes.2020.109434
30. Marchese G, Lorusso M, Parizia S et al (2018) Influence of heat treatments on microstructure evolution and mechanical properties of Inconel 625 processed by laser powder bed fusion. Mater Sci Eng A 729:64–75. https://doi.org/10.1016/j.msea.2018.05.044
31. Wang YM, Voisin T, McKeown JT et al (2018) Additively manufactured hierarchical stainless steels with high strength and ductility. Nat Mater 17:63–71. https://doi.org/10.1038/nmat5021
32. Leicht A, Klement U, Hryha E (2018) Effect of build geometry on the microstructural development of 316L parts produced by additive manufacturing. Mater Charact 143:137–143. https://doi.org/10.1016/j.matchar.2018.04.040
33. Sofinowski KA, Raman S, Wang X et al (2021) Layer-wise engineering of grain orientation (LEGO) in laser powder bed fusion of stainless steel 316L. Addit Manuf 38:101809. https://doi.org/10.1016/j.addma.2020.101809
34. Dantzig JA, Rappaz M (2009) Solidification, 1st edn. EPFL Press, Lausanne
35. Hu YL, Lin X, Zhang SY et al (2018) Effect of solution heat treatment on the microstructure and mechanical properties of Inconel 625 superalloy fabricated by laser solid forming. J Alloys Compd 767:330–344. https://doi.org/10.1016/j.jallcom.2018.07.087